AFRL-AFOSR-VA-TR-2024-0107

Pockets in highly turbulent premixed flames: physics and implications on modeling

Xinyu Zhao
UNIVERSITY OF CONNECTICUT
438 WHITNEY RD EXTENSION UNIT 1133
STORRS, CT, 06269
USA

01/18/2024
Final Technical Report

Air Force Research Laboratory
Air Force Office of Scientific Research
Arlington, Virginia 22203
Air Force Materiel Command

REPORT DOCUMENTATION PAGE

PLEASE DO NOT RETURN YOUR FORM TO THE ABOVE ORGANIZATION.

1. REPORT DATE	2. REPORT TYPE	3. DATES COVERED	
20240118	Final	START DATE 20180401	END DATE 20230929

4. TITLE AND SUBTITLE
Pockets in highly turbulent premixed flames: physics and implications on modeling

5a. CONTRACT NUMBER	5b. GRANT NUMBER	5c. PROGRAM ELEMENT NUMBER
	FA9550-18-1-0173	61102F
5d. PROJECT NUMBER	**5e. TASK NUMBER**	**5f. WORK UNIT NUMBER**

6. AUTHOR(S)
Xinyu Zhao

7. PERFORMING ORGANIZATION NAME(S) AND ADDRESS(ES)
UNIVERSITY OF CONNECTICUT
438 WHITNEY RD EXTENSION UNIT 1133
STORRS, CT 06269
USA

8. PERFORMING ORGANIZATION REPORT NUMBER

9. SPONSORING/MONITORING AGENCY NAME(S) AND ADDRESS(ES)	10. SPONSOR/MONITOR'S ACRONYM(S)	11. SPONSOR/MONITOR'S REPORT NUMBER(S)
Air Force Office of Scientific Research 875 N. Randolph St. Room 3112 Arlington, VA 22203	AFRL/AFOSR RTA1	AFRL-AFOSR-VA-TR-2024-0107

12. DISTRIBUTION/AVAILABILITY STATEMENT
A Distribution Unlimited: PB Public Release

13. SUPPLEMENTARY NOTES

14. ABSTRACT
The research project comprises two phases that focus on flame kernels in subsonic and supersonic premixed combustion environments. The objective of the first phase is to understand the underlying physical processes of two types of pockets that are observed within the thin reaction zones regime and the broken reaction zones regime, including fresh-mixture pockets surrounded by the product of the flame (termed as “FiP”) and product pockets surrounded by fresh mixtures (termed as “PiF”). Subsequently, phase II focuses on understanding the fundamental physical processes of the initiation and propagation of auto-igniting kernels within highly compressible shock-laden environment, such as in detonation. Direct numerical simulations (DNS) are employed in both phases to minimize errors arising from subgrid phenomena. During phase I, numerical experiments are designed to discern impacts of laminar flame speed and extinction strain rates on the quenching of a turbulent “PiF” flame kernel and a “FiP” flame kernel. It has been found that laminar flame speed is a critical canonical property that determines the displacement speed in strained laminar flame and in the turbulent flame studied here. The extinction strain rate plays a secondary role in determining the probability of global extinction, and reformation of fresh mixtures by quenched flame kernels is not significant enough to alter the qualitative behavior of flame kernels. Turbulence-chemistry interactions are found to be manifested through modification of the curvature stretch instead of changing tangential strain rates. Additionally, it is determined that “FiP” pockets have low probability of developing into an auto-igniting hot spot in atmospheric methane/air flames, due to the much shorter time scale of flame propagation and diffusion compared to autoignition. Extending from the phase I findings, we continue to examine the underlying physics of microscopic jets in fundamental detonation configurations where autoignition is a critical chemical mechanism in creating the induction regions. Using two-dimensional DNS of a variety of mixtures, we demonstrate that local chemical heat release alone cannot provide sufficient energy to produce an overdriven Mach stem. Instead, a virtual piston must exist to provide mechanical energy to the nascent Mach stem to produce overdrive. Through careful study of the flow field behind the Mach stem in simulation, we conclude that the virtual piston arises from fluidic jetting behind the Mach stem. The energy to drive this jet originates from the triple points and their collision, and is focused by a pair of counter-rotating vortices behind the Mach stem. Lastly, we study both subsonic flame kernels and supersonic kernels in one air force relevant application, a model rotational detonation combustor (RDC). The specific objective is to understand how flame kernels impact wave bifurcation. There we demonstrate that parasitic burning near the contact line combined with insufficient numerical resolution artificially causes wave bifurcation in RDCs. Moreover, the total number of waves cannot be predicted simply based on the inlet mass flow rates and geometry of the combustor. Local hot spots resulting from imperfect mixing can lead to wave bifurcation, which ultimately affects the wave speed and loss of the combustor.

15. SUBJECT TERMS

16. SECURITY CLASSIFICATION OF:			17. LIMITATION OF ABSTRACT	18. NUMBER OF PAGES
a. REPORT	b. ABSTRACT	c. THIS PAGE		
U	U	U	UU	48

19a. NAME OF RESPONSIBLE PERSON	19b. PHONE NUMBER *(Include area code)*
CHIPING LI	426-8574

Standard Form 298 (Rev.5/2020)
Prescribed by ANSI Std. Z39.18

Cover Sheet

Award Number: FA9550-18-1-0173
Report Type: Final
Reporting periods: Start Apr. 1, 2018 - End Sept. 30 2023
Distribution Statement: Distribution A - Approved for Public Release
Program Office Name: Dr. Chiping Li
Principal Investigator Name: Dr. Xinyu Zhao
Project Title: "Pockets" in Highly Turbulent Premixed Flames: Physics and Implications on Modeling

Abstract

The research project comprises two phases that focus on flame kernels in subsonic and supersonic premixed combustion environments. The objective of the first phase is to understand the underlying physical processes of two types of pockets that are observed within the thin reaction zones regime and the broken reaction zones regime, including fresh-mixture pockets surrounded by the product of the flame (termed as "FiP") and product pockets surrounded by fresh mixtures (termed as "PiF"). Subsequently, phase II focuses on understanding the fundamental physical processes of the initiation and propagation of auto-igniting kernels within highly compressible shock-laden environment, such as in detonation. Direct numerical simulations (DNS) are employed in both phases to minimize errors arising from subgrid phenomena. During phase I, numerical experiments are designed to discern impacts of laminar flame speed and extinction strain rates on the quenching of a turbulent "PiF" flame kernel and a "FiP" flame kernel. It has been found that laminar flame speed is a critical canonical property that determines the displacement speed in strained laminar flame and in the turbulent flame studied here. The extinction strain rate plays a secondary role in determining the probability of global extinction, and reformation of fresh mixtures by quenched flame kernels is not significant enough to alter the qualitative behavior of flame kernels. Turbulence-chemistry interactions are found to be manifested through modification of the curvature stretch instead of changing tangential strain rates. Additionally, it is determined that "FiP" pockets have low probability of developing into an auto-igniting hot spot in atmospheric methane/air flames, due to the much shorter time scale of flame propagation and diffusion compared to autoignition. Extending from the phase I findings, we continue to examine the underlying physics of microscopic jets in fundamental detonation configurations where autoignition is a critical chemical mechanism in creating the induction regions. Using two-dimensional DNS of a variety of mixtures, we demonstrate that local chemical heat release alone cannot provide sufficient energy to produce an overdriven Mach stem. Instead, a virtual piston must exist to provide mechanical energy to the nascent Mach stem to produce overdrive. Through careful study of the flow field behind the Mach stem in simulation, we conclude that the virtual piston arises from fluidic jetting behind the Mach stem. The energy to drive this jet originates from the triple points and their collision, and is focused by a pair of counter-rotating vortices behind the Mach stem. Lastly, we study both subsonic flame kernels and supersonic kernels in one air force relevant application, a model rotational detonation combustor (RDC). The specific objective is to understand how flame kernels impact

wave bifurcation. There we demonstrate that parasitic burning near the contact line combined with insufficient numerical resolution artificially causes wave bifurcation in RDCs. Moreover, the total number of waves cannot be predicted simply based on the inlet mass flow rates and geometry of the combustor. Local hot spots resulting from imperfect mixing can lead to wave bifurcation, which ultimately affects the wave speed and loss of the combustor.

ACCOMPLISHMENTS

The research project comprises two phases that focus on flame kernels in subsonic and supersonic premixed combustion environments. The primary **objective** of the first phase is to understand the underlying physical processes of two types of pockets that are observed within the thin reaction zones regime and the broken reaction zones regime, including fresh-mixture pockets surrounded by the product of the flame (termed as "FiP") and product pockets surrounded by fresh mixtures (termed as "PiF"). The existence of these pockets is a distinctive feature of flames undergoing strong turbulence and frequent local extinction. They are hypothesized to be the potential contributors to the deviation of the flame statistics from those within the flamelet regimes. In particular, we are interested in the mechanisms of local flame extinction and its relation with global flame propagation; the reforming of fresh mixtures by the "PiF" pockets and its potential impact on the global burning rate; and the possibility and conditions of auto-ignition in "FiP" pockets.

Based on the findings in phase I, in particular on the failed auto-ignition in "FiP" pocket, the project scope is further extended beyond the regime of subsonic combustion in phase II, and exploring the initiation and propagation of auto-igniting kernels within highly compressible shock-laden environment, such as in detonation. In particular, the microscopic structure and macroscopic behavior of detonation are examined to understand the energy transfer mechanism in detonation. Direct numerical simulations (DNS) are employed in both phases to minimize errors arising from modeling unknown subgrid physics.

Major activity 1: (2018-2021) Numerical experiments are designed to discern the importance of laminar flame properties on turbulent flame kernel ("PiF") extinction. Parameters of chemical kinetic models are perturbed either to maintain identical laminar flame speed while producing different counterflow extinction strain rate or vice versa. Subsequently, DNS is conducted using a highly-parallel high-order numerical code S3D [1] with the modified chemical kinetical models, subject to identical initial and boundary conditions. Results are analyzed to quantitatively understand the key controlling parameters for subsonic flame kernel extinction.

Through careful examination of the heat release history, flame topology, displacement speed, tangential strain, flame curvature, we **find**

- The laminar flame speed determines the displacement speed in strained laminar flame and the displacement speed in the turbulent flame studied here. It is a more important canonical property compared to the extinction strain rate in determining the probability of global extinction.

- Lower extinction strain rate promotes fragmentation of the flame kernel into more sub-volumes. Smaller sub-volumes generally recede faster into itself and extinguish. Exinguished flame segments lightly reform the chemical properties of the fresh mixture, but not in a significant scale. Kernels of combustion products larger than a critical Sauter mean diameter of two thermal thickness are critical to prevent global extinction for the current configuration.

- The flames studied here are borderline broken reaction zones regime, and flame surface propagation growth/destruction is still a good indicator of overall heat release behavior.

Statistics of tangential strain rates remain similar for all cases, and are not impacted by the perturbed chemical models. Instead, turbulence-chemistry interaction (TCI) is manifested more strongly through the modification of curvature stretch of flame surfaces.

- In addition to the findings about the "PiF" kernel, we successfully designed a mixture that mimics the creation of a "FiP" pocket, based on computational analysis of the contribution of heat and radicals to the ignition propensity of such pockets. DNS results indicate low possibility of such "FiP" pockets developing into an auto-igniting hot spot in atmospheric methane/air flames, due to competition between ignition delay, flame propagation, and turbulent mixing. Turbulent mixing reduces the volume of the pocket through straining and vortex stretching, while flame propagation competes with auto-ignition in consuming fresh mixtures. The ignition delays for methane/air mixtures under atmospheric conditions are simply too long compared to the time scales of the other two processes.

Major activity 2: (2021-2023) Simulations and data analysis of gaseous detonation of regular and irregular mixtures. The specific objectives are to qualitatively and quantitatively understand the micro structure of detonation, in particular the jetting behavior, and its role in energy transfer, cell regularity, and near limit phenomena. In contrast to findings in the literature, while forward jet-driven bifurcation is most common in low specific heat ratio (γ) mixtures, the forward jet is ubiquitous to all mixtures. An unambiguous definition of the forward jet independent of bifurcation is proposed, which is a region of collimated fluid kernel behind the Mach stem traveling in excess of the instantaneous Mach stem speed. The forward jetting is hypothesized to play a key role in the energy transfer process between the heat release zone and the shock. To understand the underlying physical processes, gaseous detonation with jet fuels and hydrogen through straight channels are simulated using a highly-parallelable code Athena-RFX [2]. Significant findings have been made by graduate student Patrick Meagher through close collaboration with Prof. Alexei Poludnenko at University of Connecticut and with Prof. Hai Wang at Stanford. Major findings include

- We demonstrate that local chemical heat release alone cannot provide sufficient energy to produce an overdriven Mach stem. Instead, a virtual piston must exist to provide mechanical energy to the nascent Mach stem to produce overdrive.

- Through careful study of the flowfield behind the Mach stem in simulation, we conclude that the virtual piston arises from fluidic jetting behind the Mach stem. The energy to drive this jet originates from the triple points and their collision, and is focused by a pair of counter-rotating vortices behind the Mach stem.

- To advance our understanding of cellular detonations (cell regularity, limits, etc.), focus should be shifted from a simple blast description to a more detailed understanding of the essential flow features (jets, vortex pairs), and the momentum and energy transfer processes before and after jetting.

- For the mixtures studied, the postshock ratio of specific heats γ_{VN} and mixture effective non-dimensional activation energy ϵ_i are found to be key parameters determining the

detonation cell regularity. Secondary factors (e.g. local heat release) produce minor, but discernable, variations in cell regularity for mixtures with similar γ_{VN} and ϵ_i. γ_{VN} has a substantially smaller impact on cell regularity than ϵ_i: detonation cells become slightly irregular toward a lower γ_{VN} value. In agreement with previous findings, irregularity begins to be observable when γ_{VN} crosses below the value of 1.3. The emergence of irregularity is accompanied by the onset of Mach stem bifurcations caused by jetting.

- For 2D JP10 detonation, irregular cellular features, e.g., transverse detonation, burning "finger", were observed, similar to those observed in ethylene-air detonation. Strong transverse detonations occur on average every four detonation cell cycles, and lead to large variations, up to 50%, in global heat release rate. Comparison of 2D and 3D show that both the cellular structure and global burning can be drastically different in 3D.

Major activity 3: (2021-2022) Effects of both subsonic and supersonic hotspots in air-force relevant rotation detonation combustors are studied lastly. Numerical resolutions in rotating detonation combustors are low in the literature, constrained by the size of the combustor, scale separation, and computational cost. In-house solvers with adaptive mesh refinement (AMR) and dynamic load balancing (DLB) are developed within the framework of OpenFOAM [3] to enable accurate simulations of RDC. The specific objective is to study the conditions under which hot spots lead to wave bifurcations in RDC.

- The number of waves in RDCs is not a unique function of the inlet boundary conditions and geometry; it is impacted by the number of hot spots that may result from imperfect mixing (physically) and/or insufficient resolution and numerical diffusion (numerically).

- In addition to heat and viscous loss through wall boundaries, pressure drop along the axial direction is an additional loss mechanism that reduces wave speed. Number of waves, mass flow rates of fuel/oxidizer mixtures, geometry of the RDC are intricately connected to determine the total loss.

- Numerically, one-level AMR with dynamic load balancing can effectively reduce the computational cost by 70% for a single-wave RDC combustor simulation. Without load balancing, the reduction in computational cost is only 30%. For AMR up to two levels of refinement, optimal performance is achieved when approximately 18,000 cells per core are maintained.

Results dissemination. Findings from all major activities are disseminated through archived journal publications [4, 5, 6, 7] and national and international conferences [8, 9, 10, 11, 12, 13, 14, 15, 16, 17, 18, 19]. Results from this project are also presented during an outreach event called "Space Expo" at the New England Air Museum in 2021 to enhance public understanding and increase interest in learning and careers in science, technology and humanities.

IMPACTS

Development of the principal discipline of the project.

- Key laminar flame properties, including flame speed, ignition delay and extinction strain rates, are well understood in the combustion community. However, significant gap exists between the understanding of turbulent flame extinction and its connection to well-established laminar flame properties. The study of the extinction subsonic flame kernel bridges the understanding between turbulent flame extinction and laminar flame extinction, through carefully designed numerical experiments. For the first time, we delineate how the laminar properties impact turbulent flame behaviors and identify critical parameters for flame kernel propagation and extinction. These findings can lead to insights in how to manipulate flame propagation and extinction for modern aeronautical engines.

- The study of the jetting behavior of gaseous detonation revolutionizes the microscopic view of detonation structure and propagation. For the first time, the virtual piston created by the jetting phenomenon is identified to be the driving mechanism for cell initiation. The traditional blast theory has been shown to be inadequate as a theory to describe the cellular structures of detonation and we demonstrate that contradictory to traditional belief, chemical reactions alone cannot provide sufficient energy during the onset of a new detonation cell. The findings in this project suggest a future research direction that has been overlooked and less examined in the past few decades.

- The rotational detonation combustor study extends insights from fundamental deflagration and detonation to more realistic air-force relevant applications. The hotspots, either physically or numerically created, are found to lead to wave bifurcations in RDCs, which subsequently impacts wave speed and loss of RDC through impacting pressure gradients. The adaptive mesh refinement and dynamic load balancing toolbox created in this project opens doors to more realistic air-force relevant simulations in the future.

Impact on teaching and educational experience.

The project funded two graduate students through their Ph.D. in mechanical engineering. The projects provide ample opportunities for the graduate students to interact with collaborators and experts in the field through various virtual group meetings and international/national conferences. In particular, the project enables graduate student Patrick Meagher to visit Prof. Hai Wang's lab at Stanford and work under his direction for an extended period of time, which is an extremely valuable experience for his professional development. The project also provides them other professional training opportunities in addition to the research experience. For example, Patrick has become a main organizer of the Young Scholar Detonation Forum after only 2.5 years of working on detonation and has participated in more than ten national and international conferences during his career at UConn.

The project provides a large amount of data and animations with rare precision. The animations and data have been employed in the PI's "Introduction to Computational Fluid Dynamics" Class, as examples and resources for undergraduate students who had no prior experience of CFD. The data are also employed as numerical examples in a textbook that the PI is writing entitled "Heat transfer explained: a computational perspective", which is expected to be published in 2025.

Impact on society beyond science and technology.

Understanding extinction of turbulent combustion is critical in designing modern gas turbine engines that are compatible with sustainable fuels to meet zero-emission goals in the near future. On the other hand, detonation is one of the most efficient ways of energy production that is particularly compatible with hydrogen, which is a clean and sustainable form of fuel to cope with climate change. If successful, the environmental impact would benefit everyone on this planet, and certainly alter regulatory policy and energy consumption behavior of the future generation.

CHANGES

Rebudget was implemented in 2022 to support the visit of Patrick Meagher at Stanford University. The reduced personnel support has been compensated by the enhanced productivity of Patrick during his close collaboration with Prof. Wang's lab.

TECHNICAL UPDATES

1. 3D DNS of Methane "PiF" Pockets: Extinction Mechanism

A previous JP-8 kernel study from the PI's group [20] identified two relevant extinction mechanisms for the kernel propagation problem, represented by a counterflow reactant-to-product (R2P) configuration and a counterflow reactant-to-reactant (R2R) configuration. The extent of negative displacement speed observed in the R2P configuration under high stretch conditions is closely correlated with the global extinction behavior by reducing the volume of burnt products, and the displacement speed is connected with the laminar flame speed through the Markstein length. Meanwhile, bigger flame kernels are fragmented into smaller kernels through the R2R mechanism, which can either accelerate destruction of burnt products or promote surface growth by avoiding extreme strain rates on the flame surface. Of the two, the R2P configuration is more correlated to the global extinction behavior. To further separate the roles of laminar flame speed and extinction strain rates, a few "engineered" chemical kinetic models are developed. Subsequently, 3D DNS of methane "PiF" pockets have been simulated during the previous report period using S3D, and more data analysis has been performed during the current report period.

1.1. Generation of chemical mechanisms with "engineered" properties

A Monte Carlo numerical experiment is designed to perturb the nominal chemical kinetic model for methane. The objective is to obtain "engineered" kinetic models that share the same laminar flame speed but different extinction strain rates, and vice versa. A 25-species 144-reaction skeletal chemical model for CH_4 derived from FFCM-1 [21] is adopted in this study, which is further reduced to 17 species in the DNS (see Supplementary material). The pre-exponential factors are perturbed in the following manner using Monte Carlo sampling,

$$A_i = A_0 \exp(x_i \ln(f)) \ , \tag{1}$$

where A_i and A_0 are the perturbed and nominal pre-exponential factors, respectively, f is the uncertainty factor that generally ranges from one to ten [22]. Here, the uncertainty factors are fixed at ten for each reaction to maximize the distribution, and x_i is a random number that is generated from a standard normal distribution ($\mu = 0$, $\sigma = 1/2$).

Using the 680 perturbed chemical kinetic models, laminar flame speed and extinction strain rate are computed using Cantera's freely propagating flame solver and the twin-premixed counterflow flame solver [23], respectively. An in-house approach is derived to ensure accurate capture of the turning point for the twin-premixed flame calculation. The conditions are atmospheric pressure and 300 K at an equivalence ratio ϕ of 0.7. The mean and standard deviation of the perturbed laminar flame speed are $\mu_{SL} = 0.175$ m/s and $\sigma_{SL} = 0.117$ m/s, respectively. Mean and standard deviation of the perturbed extinction strain rate are $\mu_K = 1097$ 1/s and $\sigma_K = 1201$ 1/s, respectively. From these simulations, two perturbed chemical kinetic models with extreme differences in these two canonical properties are identified to test our hypotheses, including one with a high laminar flame speed but comparable extinction strain rate to the nominal case (case HLFS) and one with a low extinction strain rate but comparable laminar flame speed (case LESR). Details for the two mechanisms are provided in Table 1.

Table 1: Laminar flame speed and extinction strain rate for the nominal and perturbed mechanisms and percentage difference from the nominal.

Designation	s_l (cm/s)	Percent Difference s_L	a_{R-R} (1/s)	Percent Difference a_{R-R}
Nominal	16.93	0%	912	0%
HLFS	21.58	27.4%	978	7.29%
LESR	16.55	-2.27%	670	-26.5%

The two chemical kinetic models are compared with the nominal model using the unstrained laminar flame, the R2R and R2P configurations in Fig. 1. Progress variable c is defined based on O_2 mass fractions throughout this study. For the R2R and unstrained laminar flame configurations, both perturbed models show reduced heat release rates at $c > 0.9$ compared to the nominal model. In other words, heat release rates are more heavily weighted towards smaller progress variables for these two designed mechanisms. For the R2P configurations, the normalized displacement speed s_d/s_l at $c = 0.8$ is plotted as a function of the local strain rate. The LESR case and the nominal case have similar displacement speeds at low strain rate due to their similar unstrained laminar flame speeds. With increasing strain rate, s_d from the nominal mechanism becomes the lowest, indicating the fastest receding flame among all three cases.

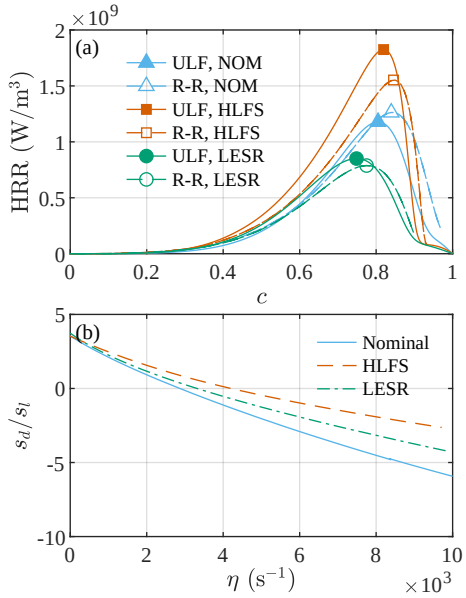

Figure 1: (a) Local volumetric heat release rate in O_2 progress variable c space for unstrained laminar flames (ULF) and R2R counterflow flames for the nominal, HLFS, and LESR cases. (b) $c = 0.8$ isosurface displacement speed s_d normalized by the unstrained laminar flame speed s_l as function of local strain rate η for R2P counterflow flames for nominal, HLFS, and LESR cases.

1.2. Configuration

A methane/air flame kernel in triply periodic cubic box is simulated in this study. A spherical product region is initialized in the middle of the computational domain, surrounded by fresh mixture. A non-reacting linearly forced [24] auxiliary DNS is first conducted until the turbulent kinetic energy spectra converged after approximately 30 eddy-turn over times. The turbulent fluctuating velocity and integral length scale are specified to be $u' = 10.0$ m/s and $L_T = 4$ mm, respectively, for a turbulent Reynolds number of $Re_T = 2500$. This results in an eddy turnover time of $\tau = 0.4$ ms. The associated Kolmogorov length scale is $L_\eta = 11.3$ μm, and the Kolmogorov velocity scale is $u_\eta = 1.42$ m/s. This yields a Damköhler number $Da = 0.94$ and Karlovitz number $Ka = 535$. The initial spherical flame kernel is generated by superimposing temperature and species profiles calculated from an unstrained laminar flame using the nominal chemical mechanism. The radius of the spherical kernel, defined as the distance from the center of the domain to $|\nabla T|_{max}$ is kept constant between all cases at $r = 6.36\delta_{nom}$ where δ_{nom} is the thermal flame thickness for the nominal model.

S3D [25] is employed to conduct all DNS in this study. The cubic computational domain has an edge length of $L = 5L_T$. The domain is discretized into a uniform $896 \times 896 \times 896$ mesh with a grid spacing of Δ =22.5 μm for all cases, which equates to $\Delta \approx 2L_\eta$. This resolution also corresponds to 25 to 35 grid points per thermal thickness. A fixed time step of 9 ns is used for all cases, which resolves both flow and chemistry scales. All simulations employ mixture-averaged transport properties, and the Soret effect is neglected.

1.3. Detailed analysis of the flame kernels

Figure 2 shows the evolution of integrated heat release rate (HRR) over time. Two integration intervals are presented, including the full domain ($c = [0, 1]$) and the product region defined as $c = [0.8, 1]$. The adjustment of the initial conditions to the specific chemical kinetic model takes less than 0.1τ and peak HRR occurs around 0.7τ. Only the HRR from the HLFS case is substantial after five eddy turnover times (2 ms). The LESR case survives slightly longer than the nominal case based on the full-domain HRR. Interestingly, the product-region HRRs are almost identical between the LESR case and the nominal case. This indicates that the heat release contribution from $c < 0.8$ is stronger in the LESR case than in the nominal case, due to differences in their heat release profiles as shown in Fig. 1(a). Nonetheless, the difference in full-domain integrated HRR is insignificant between the LESR case and nominal case, and they both have the same qualitative behavior. The integrated HRR in the $c = [0.8, 1]$ region follows the full-domain trend closely, and hence the $c = 0.8$ isosurface is chosen to be analyzed subsequently.

The evolution of the $c = 0.8$ progress variable iso-surfaces is illustrated in Fig. 3 at one and three eddy turnover times, colored by instantaneous heat release rates. At time τ, the shapes of the isocontours from all three cases remain similar, where the HLFS case has the strongest heat release rate on the flame surfaces. After another two eddy turnover times, apparent differences in the flame topology can be observed, where the HLFS case retains most burnt volumes with strong surface heat release rates and the nominal case has the lease amount of burnt volume. To quantify the differences between the three cases, statistics of the flame surface and volume are analyzed next.

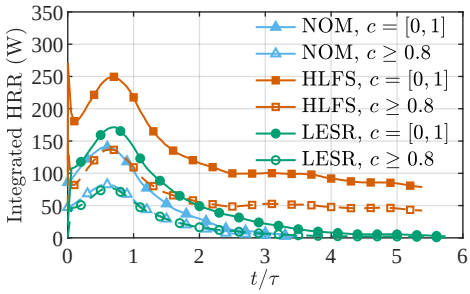

Figure 2: Integrated heat release rate for full computational domain($c = [0, 1]$), and product volume with $c \geq 0.8$.

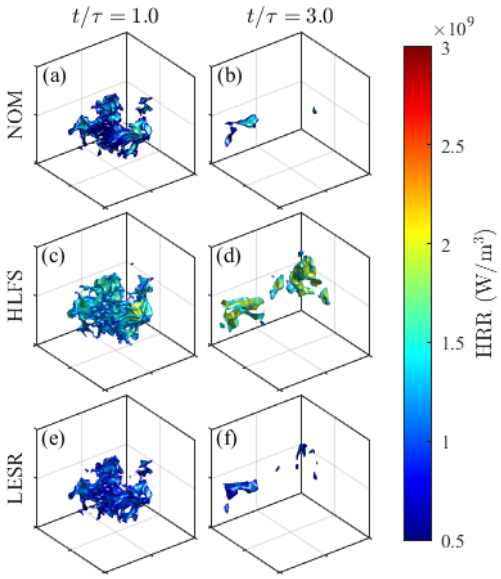

Figure 3: Evolution of the $c = 0.8$ isosurface colored by instantaneous heat release rate.

With frequent local extinction, the flame kernel is fragmented over time. The number of isolated islands at five time instances are shown in Fig. 4(a). The isolated islands are demarcated by first converting the 3D progress variable field to a discrete binary field using the condition $c \geq 0.8$. Cubic pixels are connected if any face, edge, or vertex are shared, and connected volumes are uniquely labeled. Finally, any volumes that cross a pair of periodic boundaries are merged. At time τ when burning is still vigorous for all three cases, the LESR case generates most isolated volumes, due to its smallest extinction strain rate and possibly more frequent R2R type local extinction. The nominal case shows the lowest number of isolated volume at the same time and continues to be the lowest count throughout the simulation. Since case HLFS and the nominal case have similar extinction strain rates that are higher than the LESR case, the differences in isolated volumes can be explained by the faster recession of flame surfaces (e.g., larger negative displacement speed as shown in Fig. 1) in the nominal case compared to the other two cases.

Figure 4(b) shows the sphericity ($\psi = \pi^{1/3}(6V_p)^{2/3}/A$) versus the volume ($V_p$) based diameter $d_3 = \sqrt[3]{6V_p/\pi}$, for each isolated volume from all snapshots in Fig. 4(a). Unity ψ indicates spherical shape. Generally, smaller volumes are closer to be spherical, because weakened turbulence straining at smaller scales, e.g., smaller than the Taylor microscale (0.3 to $0.5\delta_T$). Larger volumes with ψ=0.25 to 0.3 around the integral length scale (5 to $7\delta_T$) deviate much more from sphere. For example, a value of $\psi = 0.32$ can correspond to a cylinder whose height is either one tenth of its radius (i.e., a disk) or ten times of its radius (i.e., a noodle).

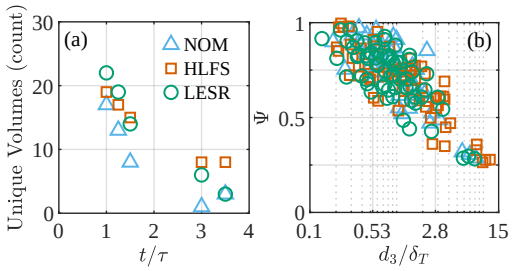

Figure 4: (a) Evolution of number of isolated product volumes through time for all three cases. (b) Sphericity Ψ as function of normalized d_3 diameter for individual product volumes.

Figure 5 further shows the global evolution of total volume V, surface area A, domain Sauter mean diameter ($\bar{d}_{32} = 6V/A$), and displacement speed s_d. Consistent with Figs. 3 and 4, the total volume and area decrease with time and eventually plateau for the HLFS case. Regardless the different counts of isolated volumes, the LESR case and the nominal case show similar rates of reduction in area up to approximately 2τ, indicating that frequent fragmentation from the LESR case does not facilitate production of flame surface areas. Therefore, the displacement speed hence the laminar flame speed is more critical a property than the extinction strain rate here in leading to global flame extinction. Most interestingly, Fig. 5(c) suggests that the critical Sauter mean diameter for flame propagation is twice the laminar thermal thickness δ_T, which is much smaller than the reported values of 22-24 from a recent experimental study of methane/air kernel ignition at lower turbulence intensities [26]. There the diameter was derived from 2D projected areas of 3D images obtained from a Swinging sheets system, and the 3D images were constructed using 74 to 78 laser images over a span of approximately 0.15 eddy turnover time. The different definitions of diameters, different turbulence conditions, and different resolutions can contribute to the differences here. It would be interesting to conduct a direct comparison with experiment as a future research avenue.

Figure 6(a) shows normalized displacement speed as function of reciprocal normalized $\bar{d}_{32}$ for each isolated volume for all five time snapshots. In general, the displacement speed decreases with decreasing $\bar{d}_{32}$, indicating that flame surfaces from smaller volumes generally recede faster than those of larger volumes. Linear trends are observed for all three chemical kinetic models. Trend lines for each set of data are also shown in Fig. 6(a), the fitted functions of which can potentially be used in modeling studies. All three cases show similar trends at larger $\bar{d}_{32}$ (smaller $\delta_T/\bar{d}_{32}$). Figure 6(b) shows normalized displacement speed as function of the area-weighted averaged total stretch rate η for each sub-volume. A non-linear trend is observed relating the

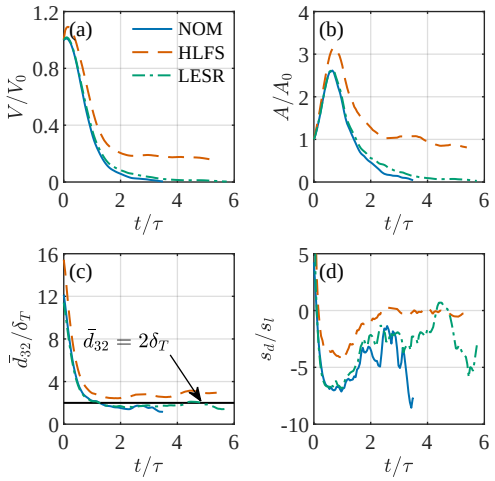

Figure 5: Evolution of $c = 0.80$ progress variable isosurface through normalized time t/τ. (a) Volume V with $c \geq 0.80$ normalized by initial kernel volume V_0. (b) Area A of $c = 0.80$ isosurface normalized by initial kernel surface area A_0. (c) Domain Sauter mean diameter $\bar{d}_{32}$ normalized by flame thickness δ_T. (d) Area weighted isosurface displacement speed s_d normalized by laminar flame speed s_l.

displacement speed and the negative stretch rate, which deviates from the steady mild-stretch Markstein-length based relation [27] due to the relatively high Reynolds number and Karlovitz number in this study.

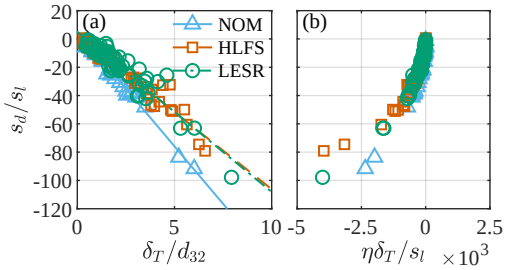

Figure 6: Normalized mean isosuface propagation speed s_d/s_l for isolated product volumes identified in Fig. 4(a) as function of (a) reciprocal of normalized Sauter mean diameter d_{32}/δ_T, and (b) normalized total stretch rate $\eta\delta_T/s_l$. For (a), a curve fit of form $(s_d/s_l) = A(d_{32}/\delta_T)^{-1} + B$ for each case is plotted. A values are -16.2634, -10.9044, and -11.3108, B values are 5.4248, 2.8642, 4.9441, for cases NOM, HLFS, and LESR, respectively.

To understand the response of the flame surfaces to turbulence, Fig. 7 shows the evolution of area-averaged curvature, curvature stretch, tangential strain rate, and total stretch rate (same definitions as in [20]) for all three cases. Higher averaged curvature appears after approximately one eddy turnover time in the LESR case and the nominal case. The curvature stretch follows similar trend as the curvature, with slight deviation after one eddy turnover time. Regardless of the geometrical differences, the tangential strain rate remains very comparable between one another until three eddy-turnover times, after which burnt volumes in the nominal and the LESR cases quickly diminish and the tangential strain rates drop to zero. The tangential strain rate has a dominate contribution to the total stretch rate upto approximately one eddy turnover, while the curvature stretch takes over and become the dominant component after that for the

LESR and nominal cases. The turbulence intensities from all three cases are comparable over the entire simulation window, and the trend of the tangential strain rate indicates that turbulent flow field is the deterministic factor contributing to the tangential strain rates. Differences in curvature result from differences in flame topology and displacement speed, both arising from differences in chemical properties.

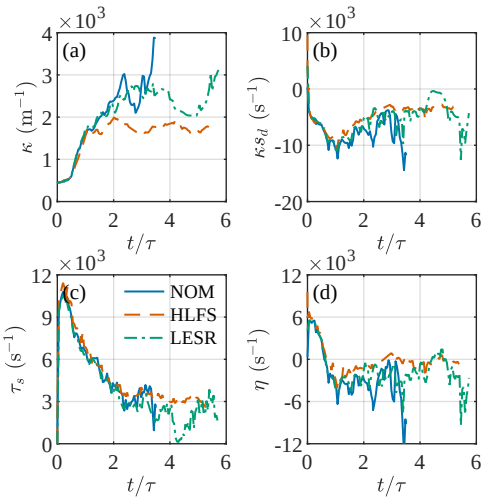

Figure 7: Area weighted (a) average curvature κ, (b) curvature stretch rate κs_d, (c) hydrodynamic strain rate τ_s, and (d) total stretch rate η of $c = 0.80$ progress variable isosurface through normalized time t/τ.

1.4. Summary

DNS of methane/air flame product kernels subject to isotropic homogeneous turbulence are conducted in this study. A reduced methane/air chemical kinetic model is employed to provide the baseline results, and two "engineered" chemical kinetic models are derived using Monte Carlo sampling to match either the laminar flame speed or extinction strain rate with the baseline case, while maintaining other flame properties. The flame kernel with the largest laminar flame speed survives until the end of the simulation, while the other two cases extinguish approximately before four eddy turnover times. The following observations are made by examining flame topology, surface statistics and chemical characteristics.

- Lower extinction strain rate promotes fragmentation of the flame kernel into more sub-volumes. Smaller sub-volumes generally recede faster into itself. Significant volumes of combustion products larger than a critical Sauter mean diameter of two thermal thickness are critical to prevent global extinction for the current configuration.

- The laminar flame speed determines the displacement speed in strained laminar flame and the displacement speed in the turbulent flame studied here. It is a more important canonical property compared to the extinction strain rate in determining the probability of global extinction.

- The flames studied here are borderline broken reaction zones regime, and flame surface propagation growth/destruction is still a good indicator of overall heat release behavior.

Turbulence-chemistry interaction is manifested more strongly through the modification of curvature of flame surfaces. Tangential strain rates remain similar for all three cases, and are not impacted by the different chemistry.

2. Microscopic fluid jetting as the origin of detonation cell

2.1. Introduction

Cellular detonations propagate in a pulsing and cyclic manner: the formation of a detonation cell begins with a triple-point collision emanating a new shock wave that propagates at a speed initially faster than the Chapman-Jouguet (CJ) speed. This overdriven wave propagates forwardly into the unburned gas and outwardly from the base of the cell as it gradually weakens to an underdriven wave while it is encroached and eventually overtaken by the spatially adjacent overdriven waves. The death of a cell coincides with the completion of one cycle of cell formation, but at which point, a new triple point collision occurs, leading to a new cell cycle. The detonation cell cycle concept [28, 29, 30, 31, 32] is supported by a range of experimental observations, including triple point structure and collisions [33, 34, 35, 36], wave front speed measurements revealing the overdriven to underdriven transition [37, 28, 29, 38], and local reaction zone structures [39, 40]. While the cell cycle theory satisfactorily links the kinematics of wave fronts to the geometry of cell pattern, the underlying physical process is yet to be understood at a detailed level especially concerning the mechanisms of momentum and energy transfers before and after a triple-point collision. As a result, several key features of cellular detonation propagation remain unexplained; they include the question as to why multidimensional detonations tend to propagate at the CJ speed as predicted by simple one-dimensional treatment of mass, momentum and energy conservation.

In this current study, we propose a new description of the detonation cycle based on microscopic, high-speed jetting that emerges immediately after triple-point collisions. We argue that jetting, a high-speed fluid motion, is the fundamental mechanism that drives cellular detonation propagation. Jetting is known to occur during Mach reflections [41], and has been observed in both non-reacting and reacting flow scenarios, e.g., shock reflection over a wedge [42, 43], near-limit detonation [33], detonation initiation following reflection of a quenched detonation [44], and collision of two quenched detonations [45]. To date, the role of jetting in governing the behaviors of cellular detonation remains largely unknown. Previous studies focused on the convective motion of jetting leading to its interaction with Mach stem and enhanced mixing. Radulescu et al. [46, 47] proposed that the interaction between strong jetting and Mach stem could lead to the Mach bifurcation phenomenon where a new transverse wave and the corresponding triple point are generated. It was further argued that the jetting-led vortex behind the Mach stem acts to enhance mixing between burned and unburned mixtures and therefore promotes reaction and energy release. As such, jetting has also been proposed as an effective means to enable deflagration to detonation transition [48, 49]. Despite significant effort expended studying these fluid jets, knowledge is still lacking in two key areas. First, the role of energy transfer via the fluidic jet in the propagation of cellular detonations remains unclear. Second, the detailed mechanism by which these fluidic jets are formed behind the nascent Mach stem remains to be understood.

The role of fluidic jetting and its generation mechanism are explored via analytical and simulation efforts. Simulations were conducted in `Athena-RFX` as outlined in Ref. [50]. We focus on a single mixture comprised of $2H_2$–O_2–CO_2 with 9000 PPM of O_3 added to produce a regular detonation structure. Previous work has validated this simulation against experimental measurements for the same mixture [50]. We will first review the fundamentals of the detonation cellular structure, and establish the essential role of the mechanism by which the Mach stem is formed and becomes overdriven. Second, we will show through simplified thermodynamic analysis that a virtual piston is required to provide energy to the nascent Mach stem. Finally, we show that this piston originates from a high-speed fluidic jet located behind the Mach stem. This jet is driven by a pair of counter-rotating vorticies that compress and accelerate the fluid into the Mach stem, and provide the energy to overdrive the Mach stem.

2.2. The detonation cell

The key feature of a detonation is the detonation cell, with an ensemble of cells giving rise to the ubiquitous cellular structure. In Fig. 8(a), we briefly review the structure of the detonation in the context of the cellular structure. The orange shaded region highlights a single detonation cell. Inside the detonation cell, a single forward propagating shock wave is present, referred to here as the Mach stem. Along the perimeter of the cell, the Mach stem shock intersects with the adjacent detonation frontal waves, or the incident shocks. By tracking the point of this intersection (indicated by the dashed lines on the perimeter of the cell), the detonation cell is drawn. The intersection of these shocks draws the fish scale pattern typical of soot foils in experiments, and numerical soot foils in simulation.

The evolution of the Mach stem is illustrated by the normalized speed of the Mach stem D/D_{CJ} along the centerline A–A, provided below the schematic. The Mach stem is first born at ①. In this moment, the Mach stem from the previous cell is completely overtaken by the faster moving incident shocks (Mach stems of neighboring cells) above and below the centerline A–A. These two incident shocks interact, and a new Mach stem is born. Initially from ① to ②, the Mach stem undergoes a rapid acceleration to become overdriven, before decaying in the later portion of the cell ②–③. The geometry of the three waves (Mach stem and two incident shocks), as well as their relative speeds and decay rates, are what give rise to the cell shape.

The geometry of a detonation cell, particularly the cell length ℓ or width λ, has been a major focus of researchers for six decades [51]. The most popular approaches to estimate the detonation cell size track the kinematics of the Mach stem and incident shocks, estimating a triple point trajectory from which cell dimensions can be computed [30, 32, 52]. Critical to these approaches is the Mach stem speed, which is typically parameterized by an initial overdrive factor (i.e. D/D_{CJ} of the nascent Mach stem). The initial overdrive and evolution of D is modeled some variation of the blast theory, illustrated in Fig. 8(b). Restated briefly, the blast theory proposes that the unburnt *keystone* left behind by the decay of the previous cell is responsible for the formation of the overdriven Mach stem. The keystone is compressed by transverse waves emanating from the intersection of the incident shocks and Mach stems, i.e. triple points. This compression triggers a local explosion, and the rapid heat release from chemical reactions produces acoustic waves which give rise to and strengthen the Mach stem.

Reenvisioning the origin of the detonation cell, contrary to the blast model, we propose that the origin is hydrodynamic. In this model, energy is provided to the nascent Mach stem by a

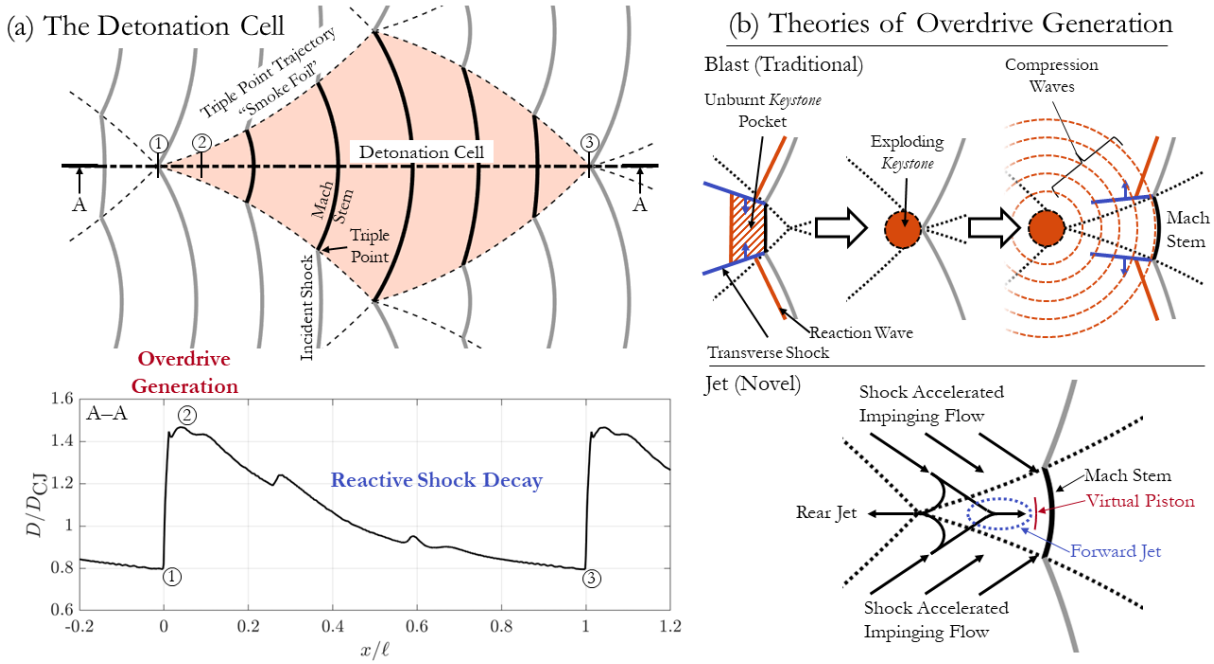

Figure 8: (a) Schematic of the detonation cell, and the frontal velocity of the Mach stem throughout the life of the detonation cell from numerical simulation. A single detonation cell is highlighted in orange. (b) Schematics of the traditional blast theory of detonation and the novel hydrodynamic jetting mechanism demonstrated in this study.

microscopic fluidic jet originating behind the Mach stem. The stagnation of this jet behind the Mach stem acts as a virtual piston, providing the necessary energy to drive the Mach stem at speeds in excess of the CJ speed. The fluid comprising the jet is compressed and accelerated by the two transverse waves, focusing the flow toward the center of the new cell. The existence of Mach stem bifurcations [46, 47, 53, 54, 50] indicates that for at least a subset of detonable mixtures, hydrodynamics play a key role in the formation and evolution of the overdriven Mach stem. In the subsequent discussion, we will show that this conclusion can be generalized to all regular detonations, as (1) a virtual piston is required to provide the work to overdrive the Mach stem as the chemical heat release alone is insufficient, and (2) the origin of this piston is fluidic jetting along the centerline of the Mach stem.

2.3. The virtual piston model

We begin by considering the evolution of a single Mach stem, illustrated in Fig. 9(a). The first frame captures the moment when the previous Mach stem vanishes, and the two incident shocks just intersect. Immediately following this, a nascent Mach stem is formed, apparent in the second frame, and this Mach stem continues to expand into the third frame. Despite the complex flow features outside of the wedge-shaped region indicated by the red dashed lines, the indicated region near the center of the Mach reflection maintains approximate radial symmetry, particularly the region of flow in front of the high speed ($v_x/D_{\mathrm{CJ}} > 1.5$) fluidic jet.

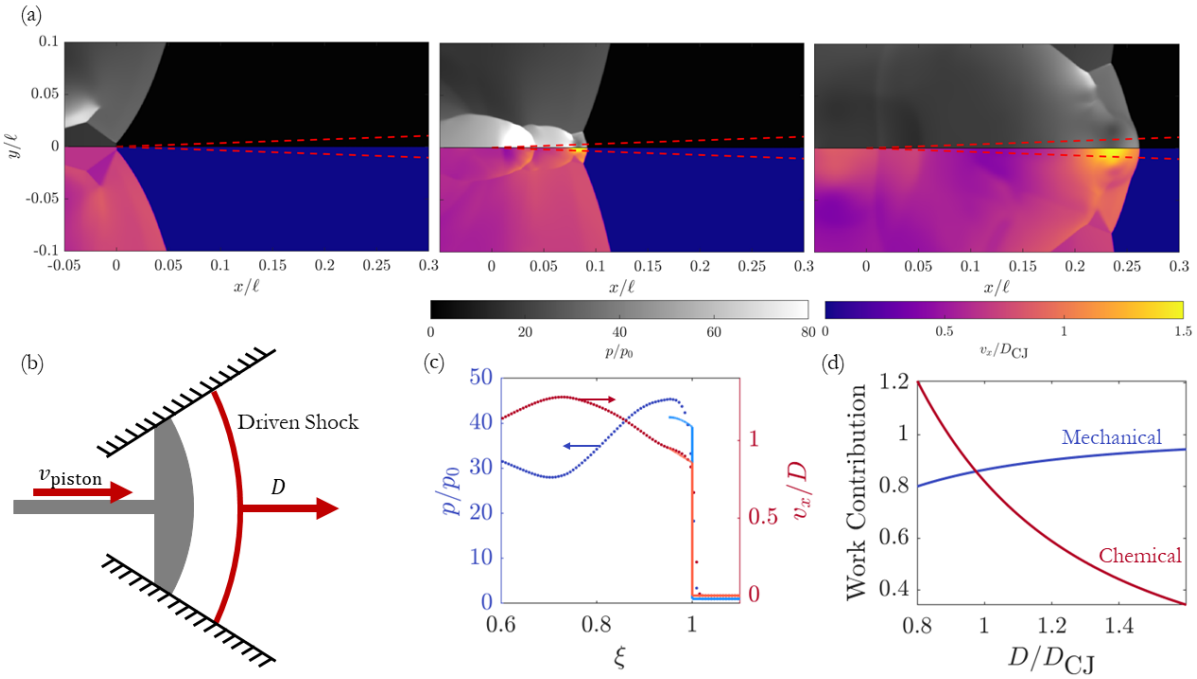

Figure 9: (a) Evolution of pressure and gas velocity during nascent Mach stem formation. The red dashed lines indicate the region of assumed self-similar flow. (b) Simple schematic of the piston-driven cylindrical expanding shock wave. (c) Comparison of similarity solution (lines) and simulation (markers) for both pressure and gas velocity along the centerline of the detonation cell. (d) Comparison of mechanical and chemical energy contributions to the piston-driven cylindrical shock.

Leveraging this radial symmetry, we developed a simplified model to capture the essential thermodynamics of the Mach stem evolution, shown schematically in Fig. 9(b). Starting with the Euler equations in cylindrical (or spherical in the case of a 3D detonation) coordinates, we assume the existence of a similarity variable $\xi = x/D(t)$, where $\xi = 1$ indicates the shock location and $\xi = 0$ is the center of the radial symmetry. $D(t)$ describes the time evolution of the speed of the driven shock. This yields a system of coupled ordinary differential equations for density, gas velocity, and pressure in ξ. We make two additional simplifying assumptions. First, we assume the gas to be inert. Second, we assume the leading shock to be approximately steady, such that $D(t)$ (simplified to D) is constant. Auxiliary calculations have shown both of these assumptions to be reasonable.

Of note in both the model and the simulation results is the negative gradient of both gas velocity and pressure. In the case of a Sednov or a similar blast wave, one would find the maximum gas velocity and pressure to be coincident with the leading shock. Here, in the piston-driven model, the maximum in both pressure and gas velocity is located at the piston face, not at the lead shock. This observation in simulation alone demonstrates the deficiency of blast theory to capture the origin and evolution of the Mach stem.

Finally, to evaluate the contributions of both chemical heat release and the work done by the

virtual piston on the nascent Mach stem, we perform a simple energy budget analysis. To do this, we compute the change in the energy stored between the piston face and the Mach stem,

$$\dot{E} = 12\pi D^3 t^2 \int_{\xi_p}^{1} (c_v T + \frac{1}{2} v^2) \xi^2 d\xi, \tag{2}$$

where ξ_p refers to the location of the piston face (contact surface) in the similarity solution. The remaining symbols t, c_v, T, and v refer to time, specific heat at constant volume, temperature, and gas velocity, respectively. The change in energy storage $\dot{E}$ is compared with the work done by the virtual piston,

$$\dot{W}_p = 4\pi D^3 t^2 \xi_p^3 p_p, \tag{3}$$

where p_p is the pressure on the piston face. Finally, to estimate the available chemical energy, we assume that the mixture instantly burns to completion while transiting the shock wave, and the heat of combustion is given by the CJ heat release for the same mixture. Thus, the energy available from chemical heat release is,

$$\dot{Q}_{\text{chem}} = 4\pi D^3 t^2 \rho_0 Q_{\text{CJ}}, \tag{4}$$

where ρ_0 is the quiescent gas density, and Q_{CJ} is the heat of combustion in mass units.

Normalizing Eqs. 3 and 4 by Eq. 2, the dependency on time and shock speed are removed. We then sweep through the range of typical Mach stem speeds in a detonation, $D/D_{\text{CJ}} \approx 0.8 \sim 1.6$, and plot the balance of mechanical work $\dot{W}/\dot{E}$ and available chemical energy $\dot{Q}/\dot{E}$ in Fig. 9(d). In the region of interest for the formation and early evolution of the Mach stem ($D/D_{\text{CJ}} \geq 1.4$), it is clear that mechanical energy via the virtual piston dominates, exceeding twice the maximum energy contribution of chemistry at high levels of overdrive. As expected, as the Mach stem approaches the CJ speed, chemical energy becomes similar to and eventually exceeds the contribution of the virtual piston. Nevertheless, this simplified thermodynamic analysis is sufficient to prove that the nascent Mach stem can only be produced by a virtual piston, and that chemical heat release alone cannot provide the energy necessary to generate the overdrives typical of detonations.

2.4. The hydrodynamic origin of the detonation cell

It has been shown that (1) the overdriven Mach stem is the necessary condition for cellular detonation propagation and (2) the overdriven Mach stem can only arise if a virtual piston drives the shock forwards. Finally, Fig. 10 demonstrates the hydrodynamic origin of the detonation cell. Particularly, a pair of counter-rotating vorticies produce a high-speed fluidic jet, converting the kinetic energy originating at the triple point into pressure in the form of the virtual piston driving the Mach stem.

Figure 10(a) is colored to illustrate the computed vorticity field from the simulation results. Superimposed on this is the instantaneous velocity field in the CJ frame, indicated by black arrows. Arrows for the quiescent gas are omitted. Figure 10(b) shows the normalized gas velocity in the laboratory frame. Finally, Fig. 10(c) provides a schematic of the flow field behind the Mach stem. It is obvious that from Fig. 10(a) that a pair of counter-rotating vortices exist behind the Mach stem, each denoted as a side vortex in the schematic. The kinetic energy

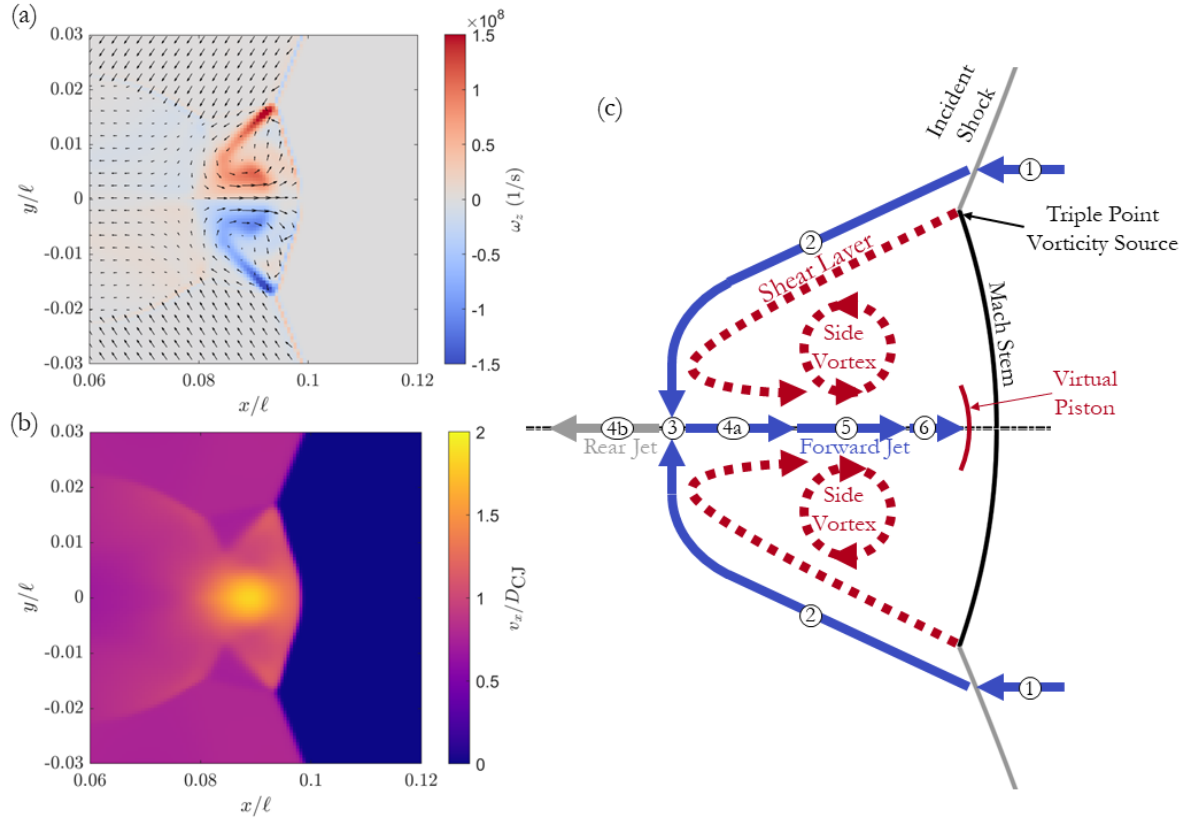

Figure 10: (a) The instantaneous velocity field in the CJ frame behind the leading shock superimposed over the computed vorticity field from 2D simulation. (b) Gas velocity behind the Mach stem showing the high speed fluidic jet driving the Mach stem. (c) Schematic of vortex/jet structure which provides energy to the Mach stem.

used to drive the vortices originates at the triple point. As a consequence of the three shock structures, a shear layer separates incoming fluids into two parts: One transits through the Mach stem and the other transits through the incident and transverse shock waves. The fluid on the Mach stem side is convected along the shear layer, until it is deposited into one of the two side vortices.

The path indicated by blue arrows in the schematic Fig. 10(c) shows the evolution of fluid elements which form the virtual piston. The quiescent unshocked gas ①, first transits through the incident and transverse shock wave. It then convects along the shear layer ②, until the two fluid streams impinge on one another at ③. Here, the flow bifurcates into a forward ④a and rear ④b stream. Of particular interest is the forward stream ④a. The two side vortices produce a local low pressure at ⑤, and the higher pressure fluid in ④a accelerates into this region. In Fig. 10(b), the forward jet is observed to have gas velocities of nearly twice D_{CJ} in the laboratory frame. Clearly, the counter-rotating vortex structure is very efficient at focusing momentum and kinetic energy behind the nascent Mach stem. Finally, in ⑥ the forward jet decelerates as the pressure increases as the jet stagnates behind the virtual piston. By this

process, kinetic energy originating at the triple point is converted into dynamic pressure in the forward jet (5), before converting to static pressure at the virtual piston which provides the necessary energy to overdrive the Mach stem.

2.5. Conclusions

In this current study, the key mechanism for cellular detonations propagation is studied in detail. Specifically, the formation of overdriven Mach stems is a necessary condition for cellular detonation propagation, but the mechanism by which overdrive is generated has been historically misattributed to rapid chemical heat release. We demonstrated that local chemical heat release alone cannot provide sufficient energy to produce an overdriven Mach stem. Instead, a virtual piston must exist to provide mechanical energy to the nascent Mach stem to produce overdrive. Through careful study of the flowfield behind the Mach stem in simulation, we conclude that the virtual piston arises from fluidic jetting behind the Mach stem. The energy to drive this jet originates from the triple points and their collision, and is focused by a pair of counter-rotating vortices behind the Mach stem. Therefore, to advance our understanding of cellular detonations (cell regularity, limits, etc.), focus should be shifted from a simple blast description to a more detailed understanding of the essential flow features (jets, vortex pairs), and the momentum and energy transfer processes before and after jetting.

3. Wave dynamics in a model rotating detonation combustor (RDE)

RDEs are associated with technical challenges arising from stability and controllability, which often result from the bifurcation of detonation waves within the combustor [55, 56, 57, 58, 59, 60, 61, 62]. Such transition can be affected by injector dynamics, nonuniform mixing, parasitic contact surface burning, shear layer instability, wall curvature and combustor geometries [63, 64, 65]. A common finding in experimental studies [56, 66, 67, 68, 59] is that increasing the mass flow rate seems to increment wave numbers [69]. Understanding the dynamics of rotating detonation waves, particularly the bifurcation and multiplicity of waves, remain a challenge due to the complex internal flow field in RDEs and its close interactions with the injection process. Single/dual-wave hybrid mode can be observed within one single experimental test [68], where the spike of detonation pressure in the dual-wave mode is approximately half of that in the one-wave mode. The individual velocity of each wave drops by almost 15% after each bifurcation as observed by Bykovskii et al. [56] A larger wave speed deficit of approximately 50% [69] is reported when there are eight [60] or nine waves [57].

Wave multiplicity in annular RDEs are also reported in numerical simulations [70, 71, 72, 73, 74, 75, 76, 77, 78, 79, 80, 81]. Schwer and Kailasanath [70] conducted two-dimensional (2D) and three-dimension (3D) simulations of premixed H_2/air [82] to assess the effect of different injector configurations on the stability and performance. In their 2D simulations with a slot injection system, they found that the lower and higher mixture plenum pressure cases are more unstable than the case with an ideal injection model [83], owing to the additional unsteadiness in the fill region due to micro-injection jets. At higher pressures, shock waves propagating in the opposite direction of the main detonation wave can accelerate and form a new detonation wave. Subsequently, the two waves collide and extinguish each other repeatedly. In the 3D simulations from Yao et al. [71], the injection intervals are adjusted along the headwall to account

for nonuniform injection. The spontaneous formation of new detonation wave is successfully captured, which is induced by collisions of wave fronts. The gas intake configuration on the headwall, the stagnation of fresh mixture, and the number of initiation positions [71] are reported to affect the number of detonation wave fronts in the stable state. Sun et al. [73] performed 2D simulations of RDEs operated with premixed H_2/air mixture through injection nozzles. They observed that the new detonation wave can be induced by the heat release at the interface between the fresh premixed gas layer and detonation products. A series of 2D simulations with a 9-species hydrogen chemical mechanism [84] of RDE with separate injection of fuel and oxidizer are conducted by Zhao et al. [80] Spontaneous wave formation is observed due to mutual enhancement of an explosive hot spot and a traveling shock wave. Influences of various fuel and oxidizer compositions on the combustion mode and detonation wave bifurcation are also studied by Zhao et al. [80] It is found that the velocity deficit is reduced with increasing mixedness of the reactants. Lietz et al. [81] simulated a 3D RDE with discrete fuel and oxidizer injector orifices. Effects of varying equivalence ratios, mass flow rates and the addition of a throat at the end of the combustor are studied. Multiple waves are present consistent with the experimental measurement.

As observed in these studies, wave multiplicity can be caused by many factors, both deterministic and stochastic, including the stagnation pressure of injection system [70], the characteristics of injectors and subsequent mixing [80], the geometry of the combustor, the number of initiations [71], deflagration in the fill region and along the contact line [73], and interactions between shock waves and local hot spots [80]. Efforts have been made to predict the number of waves in the literature [64, 65, 61], although conclusive arguments are difficult to be drawn due to the convoluted factors mentioned above. To understand impact of individual physical processes on wave multiplicity, in particular the effect of increasing mass flow rates and wave numbers, a numerical experiment with an ideal premixed injection system is designed in this study. This avoids complexities arising from interactions between the mixing processes and the detonation, isolating the intrinsic multiplicity. The initiation of detonation is carefully implemented in a mode-locked fashion to avoid spontaneous development of local hot spots and wave-wave interactions. The reacting Euler equations are solved to minimize parasitic deflagration along the contact surface. Perfectly premixed fuel/air streams are employed to avoid altering the mixture reactivity arising from inhomogeneous mixing. The objective is to identify whether wave bifurcation is a fundamental feature with increasing mass flow rate and wave number, and to identify the limit wave numbers and fill height under these idealized conditions.

3.1. Details of the solver

3.1.1. Governing equations

The reactive Euler equations for mass, momentum, species and total energy are solved in the Eulerian framework, as shown in Eqs. 5–8, respectively.

$$\partial_t \rho + \nabla \cdot [\boldsymbol{u}\rho] = 0 \ , \tag{5}$$

$$\partial_t (\rho \boldsymbol{u}) + \nabla \cdot [\boldsymbol{u}(\rho \boldsymbol{u})] = -\nabla p \ , \tag{6}$$

$$\partial_t (\rho Y_k) + \nabla \cdot [\boldsymbol{u}(\rho Y_k)] = \dot{\omega}_k \ , \tag{7}$$

$$\partial_t(\rho E) + \nabla \cdot [\boldsymbol{u}(\rho E)] = -\nabla \cdot (\boldsymbol{u}p) + \dot{q}_c \ , \tag{8}$$

where ρ is the mass density, $\boldsymbol{u}$ is the fluid velocity vector, p is the pressure and Y_k is the mass fraction for species k. The non-chemical total energy E is defined by $e_s + 1/2|\boldsymbol{u}|^2$ using the specific sensible internal energy e_s. $\dot{q}_c$ is the heat release rate (HRR) that is defined by $\sum_{k=1}^{N_s} \dot{\omega}_k h^0_{f,k}$, where $\dot{\omega}_k$ is the reaction rate of the species k and $h^0_{f,k}$ is its enthalpy of formation.

The transport equations of all species are solved except for the diluent inert species (e.g., N_2 or Ar). The mass fraction of the diluent inert species is obtained by $1 - \sum_{k=1}^{N_s-1} Y_k$ to enforce mass conservation where N_s indicates the number of species. A second-order central-upwind scheme [85] with vanLeer limiter is adopted to discretize convective terms, and an explicit second-order multi-stage Runge–Kutta scheme is employed in the temporal discretization.

An in-house chemistry solver has been developed to efficiently compute the chemical source terms using an analytical Jacobian technique [86]. The chemistry solver is coupled with the hydrodynamic solver using operator splitting. Fixed time steps are used to maintain the maximum CFL number below 0.25. When running in parallel, a round-robin load-balancing technique is applied to redistribute the computational load of chemical source terms evenly to all processors. The solver has been systematically verified using one-dimensional and two-dimensional configurations [7]. In this study, an 11 species and 34 reaction hydrogen sub-model of the Foundational Fuel Chemistry Model Version 1.0 (FFCM-1) [21] is used for all simulations.

3.1.2. Introduction of AMR and DLB

Adaptive mesh refinement using octree cell refinement for hexahedral mesh is available in OpenFOAM, where one cell is split into eight cells once a local AMR sensor satisfies the preset criteria. Neighbors to the refined cells will change from hexahedral to polyhedral cells because one interface is broken into four sub-interfaces after one refinement. In OpenFOAM, the AMR criterion is quantified by a pre-defined field that can be supplied by the user. To involve multiple field or criteria as often necessary in detonation simulations, an AMR sensor S_{AMR} is proposed in the *rhoReactingCentralFoam* solver. The sensor is able to initiate mesh refinement if any field satisfies the requirements. The preset criteria for rotating detonation combustor modeling usually include normalized magnitude of pressure gradient $|\nabla p|/|\nabla p|_{max}$ (for capturing large pressure gradient across shocks), normalized magnitude of species gradient $|\nabla Y_k|/|\nabla Y_k|_{max}$ (for capturing the interface between fresh mixture and hot product near the inlet surface) and normalized heat release rate $|HRR|/|HRR|_{max}$ (for capturing the reaction zone).

Figure 11 shows the flowchart for AMR and DLB. The procedure of AMR is introduced as follows. First, the activation of AMR is determined by the AMR sensor S_{AMR} as well as a pre-defined refinement frequency (i.e. $refineInterval$ in OpenFOAM). Second, the AMR sensor $S_{AMR,c}$ at each cell center c is evaluated based on the variables defined in AMR criteria. Then, $S_{AMR,c}$ is interpolated from cell center c to its vertex v to get the vertex value $S_{AMR,v}$ using inverse distance weighting method, i.e.,

$$S_{AMR,v} = \sum \frac{1/l^i_{cv}}{\sum 1/l^j_{cv}} S^i_{AMR,c} \ , \tag{9}$$

where l^i_{cv} is the distance between cell center c of cell i and vertex v, and $S^i_{AMR,c}$ is the cell center value of AMR sensor at cell i. For an internal field, each $S_{AMR,v}$ is contributed by eight

neighbouring cells. At each vertex, a predict error function ϵ'_v is evaluate by

$$\epsilon'_v = \min(S_{AMR,v} - S_{AMR,min}, S_{AMR,max} - S_{AMR,v}) \ , \tag{10}$$

where $S_{AMR,min}$ and $S_{AMR,max}$ are pre-defined values. If $\epsilon'_v > 0$, which means $S_{AMR,v}$ is located in the refinement range or mathematically $S_{AMR,min} < S_{AMR,v} < S_{AMR,max}$, an error function ϵ_v at vertex v is equal to the predicted error function ϵ'_v, otherwise $\epsilon_v = -1$. Then, at each cell, the cell center error function ϵ_c is determined by the maximum vertex error function, i.e., $\epsilon_c = \max(\epsilon_v)$.

Thirdly, if $\epsilon_c > 0$, the cell is refined. Otherwise, the refined cell is unrefined. Mesh update is allowed once at each time step and the change of the refinement level is limited to one level within each time step. It means that mesh update has to be executed twice to achieve level $n + 2$ from original level n. The allowed maximum difference of the refinement level of two neighboring cells is one.

Lastly, when solution is mapped from parent mesh with level n to child mesh with level $n+1$ after refinement, the cell center value of the parent mesh will be assigned to its child mesh. When solution is mapped from child mesh with level $n+1$ back to their parent mesh with level n after unrefinement or coarsening, volume-averaged cell center values over all child mesh will be assigned to their parent mesh. Face values (e.g., flux) are reconstructed from the cell center value explicitly in the two-stage Runge-Kutta method in our *rhoReactingCentralFoam*.

The method of parallel computing in OpenFOAM is domain decomposition, in which simulation domain is broken into pieces and allocated to separate processors for solution. Each processor owns nearly even mesh size to guarantee a fairly economic solution. However, once AMR is used, the intensive growing mesh size due to AMR may be concentrated on small number of processors. Consequently, a load imbalance occurs and the efficient use of computational resources may be significantly reduced, because the processor with the largest mesh size becomes a bottleneck when its processed data are required by other waiting processors. The imbalance is quantified by the maximum difference between the averaged cell number and the sub-domain cell number in OpenFOAM as follows,

$$\text{Imbalance} = \max(\frac{|\overline{N}_{cell} - N^i_{cell}|}{\overline{N}_{cell}}) \ , \tag{11}$$

where N^i_{cell} is the cell number of sub-domain or processor i, and $\bar{N}_{cell}$ is the averaged cell number which is obtained by dividing the mesh size by the number of sub-domains or processors.

Dynamic load balancing is further developed in OpenFOAM-dev by the OpenFOAM team recently [3] and this is also embeded in the *rhoReactingCentralFoam* solver. Without explicit reconstruction and decomposition during simulations [87], a more efficient method is utilized by exchanging mesh and variable fields between neighbouring processors. Figure 11 shows the flowchart of dynamic load balancing in *rhoReactingCentralFoam* solver. Once the field mapping is completed during the AMR stage, the program enters DLB stage. If redistribution interval is activated and the current imbalance is larger than the pre-defined maximum imbalance, DLB is activated. A new decomposition is created which acts as a blueprint describes the location of each cell. It is further modified given any constraints. One important constraint is that child cells from one parent cell are not permitted to be assigned to different processors,

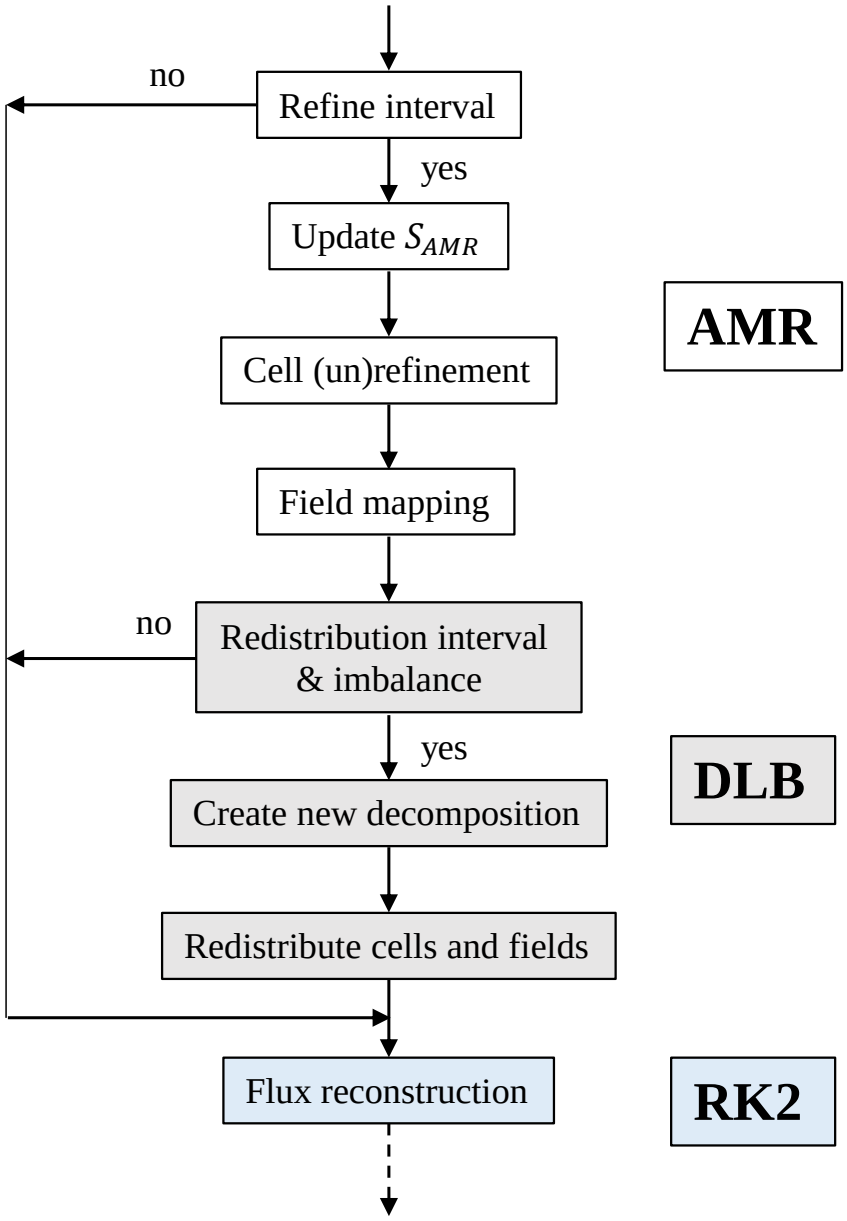

Figure 11: Adaptive mesh refinement (AMR), dynamic load balancing (DLB) and flux reconstruction in two-stage Runge-Kutta method (RK2).

which ensures that child cells are able to be merged into the parent cell when unrefinement is executed. Lastly, mesh and variable fields are sent and received between different processors. After that, the program enters into the two-stage Runge-Kutta loops.

3.2. Numerical configuration

A model annular rotation detonation combustor is constructed to study the mechanisms of wave bifurcation in RDC under ideal conditions. A schematic of the combustor geometry is presented in Fig. 12, superimposed by the initial conditions of hydrogen mass fraction Y_{H_2} and pressure p. The outer-wall diameter d_o and channel width h are 100 mm and 8 mm, respectively. The channel length L_z is 100 mm. A similar configuration can be found in [88] where $h = 10$ mm. Three numerical pressure probes, P_i, P_m and P_o are arranged at three different radial locations, r_i, r_m and r_o, respectively, close to the inlet surface ($z = 2$ mm). r_i is the inner radius, r_o is the outer radius and $r_m = 1/2(r_i + r_o)$ is highlighted by the white line on the initial pressure contour in Fig. 12.

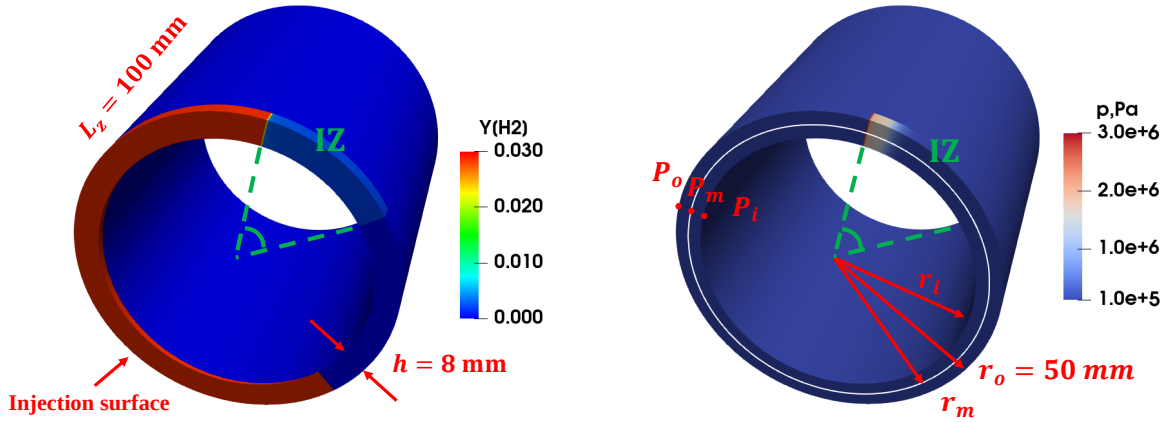

Figure 12: Geometry and initial conditions.

An ideal injection surface is designed in this study that covers the entire inlet patch. A stoichiometric mixture of hydrogen and air at a temperature T_{in} is injected into the annular combustor with a constant mass flow rate of $\dot{m}_{in}$. T_{in} and $\dot{m}_{in}$ are evaluated from the stagnation state of the total temperature T_0 and total pressure p_0. Zero gradient pressure boundary condition is applied at the inlet. The density $\rho_{in,i}$ of the inflow gas mixture for patch n on the inlet surface is determined by the ideal gas law. The inlet velocity on the local patch i can be evaluated by $U_{in,i} = \dot{m}_{in}/(\rho_{in,i}A_{in})$ where A_{in} is the area of the entire inlet surface.

The combustion chamber is initialized with cold air at the inlet temperature T_{in} and atmospheric pressure. The cold air has an initial streamwise velocity that is estimated from the stagnation state of T_0 and p_0. To ignite the mixture, a one-dimensional detonation wave structure with a height of 5 mm is superimposed onto a sub-section of the domain near the inlet surface, denoted as "IZ" in Fig. 12. A triangular fuel (H_2/air) zone is added in front of "IZ" to support continuous fuel intake to the initial detonation wave (see Fig. 12(a)). High pressure and temperature in the post-shock region are filtered to stabilize the tail of the ignition zone "IZ". Both inner and outer walls are treated as adiabatic and slip surfaces. A zero gradient boundary condition is specified for velocity, species, temperature and pressure at the outlet. Influence of the outlet boundary condition and initial conditions of ignition zone height and pressure are

examined in [7], and negligible differences are observed in the predicted pressure traces when an exhaust plenum is added to the domain or a different ignition zone height/pressure is employed.

Structured non-orthogonal hexahedral meshes are employed throughout the study. Uniform grids are specified in the radial (r) and azimuthal (θ) directions, while stretched grids are assigned in the stream-wise direction (z) to ensure better resolution near the inlet region. Table 2 summarizes all the meshes employed in this study. The coarest mesh M1 contains 1.15 million (M1) cells and three refined meshes, M2 to M4, are employed to investigate the grid dependence of the results. A baseline mesh (M1) containing 2.30 million cells is employed with the minimal resolutions in the streamwise, radial and azimuthal directions to be 0.28∼2.8 mm, 0.5 mm, and 0.36 mm, respectively.

Table 3 summarizes all the parametric cases simulated in this study. The inlet static temperature T_{in} is 250 K, which is chosen to be approximately equal to the average static temperature at the inlet when the more common total temperature inlet condition at 300 K is employed [89, 83, 90]. The baseline case, referred to as "$m/iz1/M3$", adopts a medium mass flow rate ("m", 1.16 kg/s) and one ignition zone ("$iz1$") with the mesh M3. Additional cases with inlet mass flow rates ranging from "$0.05m$" to "$5m$" are listed in the second block of Table 3. To study the impact of initial conditions on wave numbers, in the third block, two "$iz2$" to twenty-four "$iz24$" ignition zones are investigated. Each simulation is first run for 5∼7 cycles to ensure statistical stationarity, after which data is collected for another 10 to 14 cycles that contain approximately 130 snapshots.

Table 2: Summary of the mesh details.

Name	$N_z \times N_r \times N_\theta$	Δ_z(mm)	Δ_r(mm)	Δ_θ(mm)	Mesh size(M)
M1	$90 \times 16 \times 800$	0.28∼2.8	0.5	0.36	1.15
M2	$90 \times 32 \times 1600$	0.28∼2.8	0.25	0.18	4.61
M3	$180 \times 16 \times 800$	0.14∼1.4	0.5	0.36	2.30
M4	$180 \times 32 \times 1600$	0.14∼1.4	0.25	0.18	9.22

3.3. Results and discussions

3.3.1. Impact of numerical hot spots

The impact of the grid resolution on wave dynamics is first investigated using the baseline mass flow rate of 1.16 kg/s "m" and one ignition zone "$iz1$" with different grid resolutions (M1 to M4). The isocontours of temperature at successive time instances are shown in Fig. 13. All cases are initiated with identical scalar and velocity fields. For Case "$m/iz1/M1$" where the coarsest mesh M1 is applied, a small reversed detonation wave arises from the first collision between the main detonation wave and the tail of the ignition zone, as shown at $t = 0.18$ ms. Its height quickly grows before the reversed wave collides with the main detonation wave at $t = 0.21$ ms. After multiple collisions of the rotating waves subsequently, two co-rotating waves with different fill heights are sustained in the combustor annulus. Refinement in the radial and azimuthal directions in Case "$m/iz1/M2$" leads to a similar wave bifurcation process. When the mesh M1 is refined in the streamwise direction, as in Case "$m/iz1/M3$", only a single rotating wave is sustained throughout the simulation. The one-wave mode remains the same by further refining the mesh M3 in the radial and azimuthal directions (mesh M4).

Table 3: Summary of simulated cases, inflow mass flow rate $\dot{m}_{in}$, number of ignition zones N_{iz} and mesh.

Case	$\dot{m}_{in}$ (kg/s)	N_{iz}	Mesh[a]
$m/iz1/M3$ (baseline)	1.16	1	M3
$m/iz1/M1$	1.16	1	M1
$m/iz1/M2$	1.16	1	M2
$m/iz1/M4$	1.16	1	M4
$0.05m/iz1/M3$	0.06	1	M3
$0.1m/iz1/M3$	0.12	1	M3
$0.2m/iz1/M3$	0.23	1	M3
$0.5m/iz1/M3$	0.58	1	M3
$1.5m/iz1/M3$	1.74	1	M3
$2m/iz1/M3$	2.23	1	M3
$3m/iz1/M3$	3.48	1	M3
$5m/iz1/M3$	5.81	1	M3
$m/iz2/M3$	1.16	2	M3
$m/iz3/M3$	1.16	3	M3
$m/iz4/M3$	1.16	4	M3
$m/iz5/M3$	1.16	5	M3
$m/iz6/M3$	1.16	6	M3
$m/iz12/M3$	1.16	12	M3
$m/iz24/M3$	1.16	24	M3

[a] CPU hours per revolution are 270, 1600, 550, 2500 hours for mesh $M1$, $M2$, $M3$ and $M4$, respectively, which are measured on a local cluster with Haswell Xeon E5-2690 v3 CPUs.

Figure 14 presents the cell-centered values of temperature and pressure within the first layer of computational cells along the outer wall in Cases "$m/iz1/M1$", "$m/iz1/M2$", "$m/iz1/M3$" and "$m/iz1/M4$" at $t = 0.12$ ms before the first collision. An apparent difference in temperature can be found between M1 (or M2) and M3 (or M4), due to the differences in the cell height along the streamwise direction. Behind the detonation wave at $\theta = 100°$, the predicted temperature in M1 and M2 is higher than that from M3 and M4 until the temperature drops to the unburnt value at θ =140°. The maximum difference in temperature is approximately 830 K. On the contrary, the mesh resolution in the radial and azimuthal directions has negligible effects on the cell temperature when we compare the results from M1 and M2 or from M3 and M4.

The over-prediction of temperature is introduced by numerically mixing hot products with fresh mixture when the computational cell is large in the streamwise direction. In meshes M1 and M2, such a numerical hot spot is formed along the contact surface after the first collision between the main detonation and its tail, which subsequently grows and transitions to form another detonation wave propagating in the opposite direction of the main detonation wave. Subsequently, the two waves collide with one another, and wave elimination and regeneration occur frequently. Eventually, two stable waves are sustained in the chamber. However, this numerically (as opposed to physically existing) hot spot can be avoided by further refining the grid size in the streamwise direction (e.g., in meshes M3 and M4), because relatively less amount

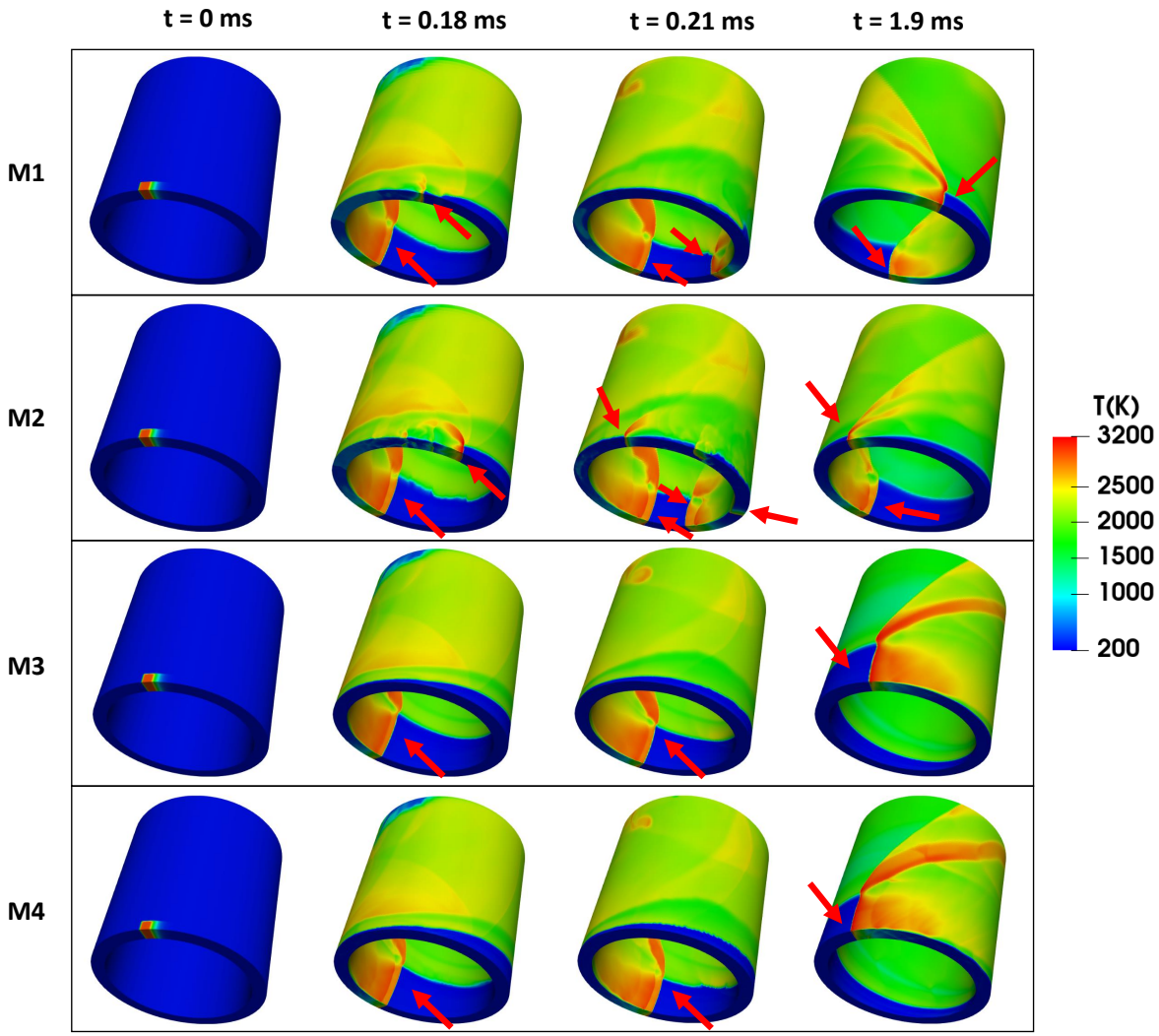

Figure 13: The contours of temperature at successive times obtained from Cases "$m/iz1/M1$", "$m/iz1/M2$", "$m/iz1/M3$" and "$m/iz1/M4$". Detonation waves are pointed by the red arrows.

of the product gas is numerically mixed with the fresh mixture near the inlet, which indicates that the bifurcation is an artifact resulting from the coarse mesh. For the 3D RDC simulation, it is critical to have sufficient streamwise resolution to capture the complex flow-chemistry coupling near the inlet, such that hot spots and wave bifurcation are not numerically introduced.

The radial and azimuthal resolutions have less impact on the temperature near the inlet, because mixing with hot products mainly occurs in the streamwise direction. Comparing Case "$m/iz1/M3$" and Case "$m/iz1/M4$", the relative difference of detonation wave speed u_D and fill height l_{cr} are 1.5% and 2%, respectively. However, finer radial and azimuthal resolutions

are necessary to capture the details of the cellular structure, as reported in Ref. [91]. Figure 15 compares the pressure contours from the first-layer cells obtained from Case "$m/iz1/M3$" and Case "$m/iz1/M4$" at $t = 1.98$ ms. In Case "$m/iz1/M4$", the detonation front moves further ahead of that on the outer wall due to a stronger expansion and compression of detonation waves captured by the finer resolution. Behind the detonation wave front, a stronger oblique shock is captured owing to the compression of the detonation wave near the outer wall and subsequently, shock trains that are established by the reflected oblique shock waves bouncing between the inner and outer walls [92] are better captured in Fig. 15(b).

Based on the resolution studies in this section, the "$M3$" mesh is chosen as the baseline and employed in all subsequent simulations. It should be noted that the grid resolution used in this study is of similar order of magnitude to prior simulations [92, 93] with similar geometries and fuels, which is not intended for capturing cellular structures or reaction zone details for hydrogen/air mixtures.

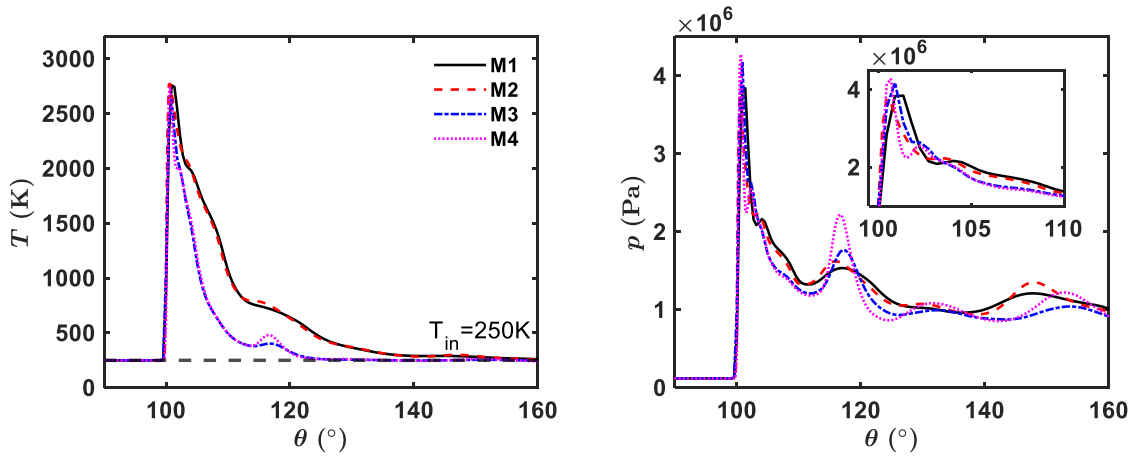

Figure 14: Cell-centered values of temperature and pressure from the first-layer cells along the outer wall obtained from Cases "$m/iz1/M1$", "$m/iz1/M2$", "$m/iz1/M3$" and "$m/iz1/M4$" at $t = 0.12$ ms.

3.3.2. Impact of inflow mass flow rates

Simulations with a range of inlet mass flow rates are conducted using the mesh M3, as listed in the second block of Table 3. All simulations observe one stable detonating wave. The fill height l_{cr} is plotted in Fig. 16(a) as function of inlet mass flow rates. The fill height increases with increasing mass flow rates and plateaus around 23∼24 mm when the mass flow rate exceeds 1.16 kg/s (Case "$m/z1/M3$"). The error bars indicate the fluctuations of l_{cr}. The fluctuations are largest at the largest mass flow rates due to a self-adjustment mechanism [72], and appear to attain smallest values when mass flow rates of 1.16 kg/s (Case "$m/z1/M3$") and 1.74 kg/s (Case "$1.5m/z1/M3$") are specified. At lower mass flow rates (Cases "$0.05m/z1/M3$", "$0.1m/z1/M3$" and "$0.2m/z1/M3$"), the fluctuations are partly caused by the wrinkled contact surface due to the Kelvin–Helmholtz instability. Figure 16(b) compares the detonation wave speed u_D and the Chapman-Jouguet (CJ) detonation velocity u_{cj} as a function of inflow mass flow rates $\dot{m}_{in}$. u_D

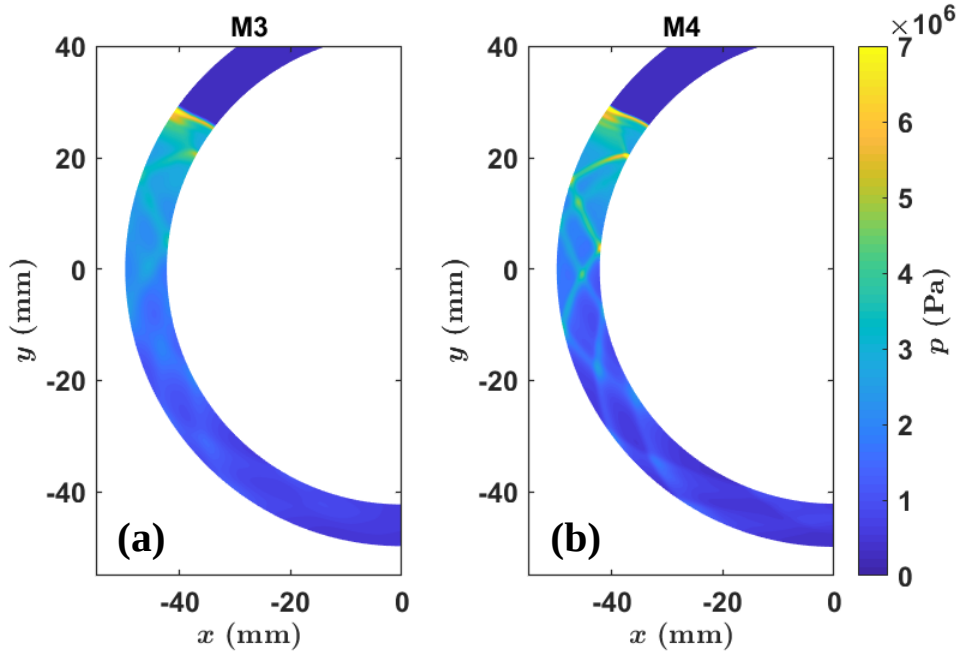

Figure 15: Iso-contours of pressure obtained from the first-layer cells from Cases (a) "$m/iz1/M3$" and (b) "$m/iz1/M4$" at $t = 1.98$ ms .

is computed by dividing $2\pi r_m$ by time intervals between peak pressure that is recorded by the pressure probes. u_{cj} is calculated based on the pre-shock pressure p_{pre} and temperature T_{pre} extracted from the locations immediately in front of the shock near the inlet patch (first-layer cell). Both velocities drop as $\dot{m}_{in}$ becomes lower, and the velocity deficit (1- u_D/u_{cj}) is maximum at lowest $\dot{m}_{in}$. The reduction of u_{cj} is due to a decrease in pre-shock pressure p_{pre}. The larger disparity between u_{cj} and u_D at lower $\dot{m}_{in}$ is further discussed in Sec. 3.3.4.

Figure 17 shows mean pressure profiles as a function of the azimuthal angle, normalized by the pre-shock pressure for each case. The profiles almost collapse into one line when the mass flow rate exceeds 0.58 kg/s (Case "$0.5m/iz1/M3$"), which corresponds to outlet conditions becoming at least partially supersonic. A modeled pressure trace proposed by Shepard and Kasahara [94] is also plotted in Fig. 17, which is described by

$$\psi(\xi) = \exp(-\beta\xi) \ , \tag{12}$$

where $\xi = x/l_{cr}$ is the distance x from the shock front normalized by the fill height l_{cr}. The parameter β is a fitting parameter, which is equivalent to the inverse of the integrated normalized pressure over ξ and $\beta = 0.96$. From fitting the pressure trace, the fill height l_{cr} is determined to be 23 mm, which is consistent with the measured values using the heat release rate.

For mass flow rates larger than 0.58 kg/s (Case "$0.5m/iz1/M3$"), $\bar{p}/\bar{p}_{pre}$ decays towards unity right before reaching the shock front at $\theta = 180°$. This indicates that the pressure expansion process takes the entire circumference to occur, which is the maximum distance x that can be supported by the current geometry. In contrast, the expansion processes are complete well

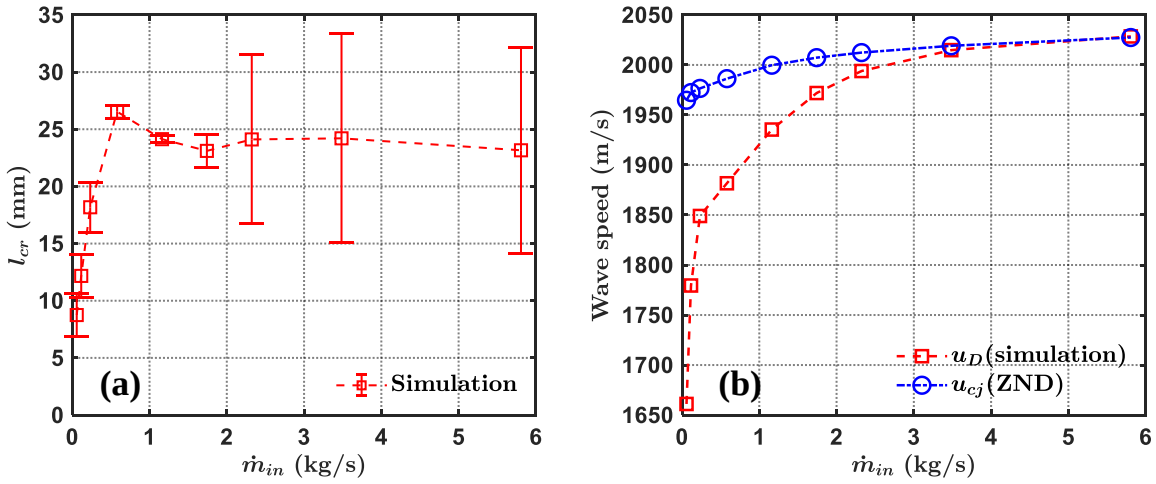

Figure 16: Variations of (a) the fill height l_{cr} and (b) detonation wave speed u_D as well as the CJ velocity u_{cj} with the inflow mass flow rate. l_{cr}, u_{in} and p_{pre} are extracted near $r = r_m$ to compute u_{CJ}.

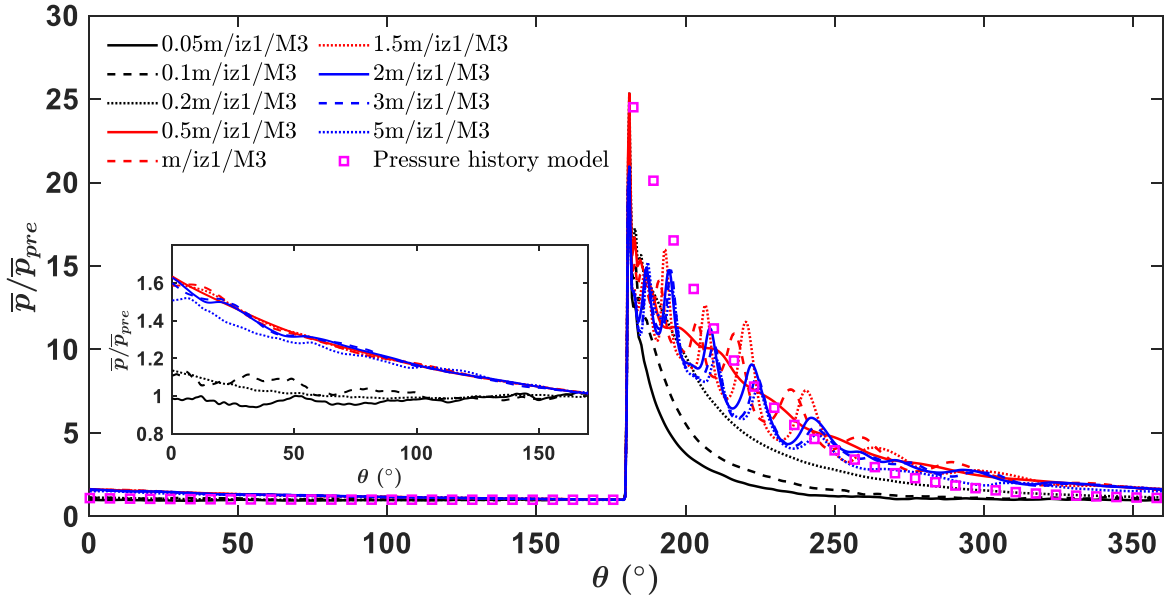

Figure 17: Normalized mean pressure profiles near the inlet patch (the first-layer cell) from the cases with different inflow mass flow rate $\dot{m}_{in}$ as well as a theoretical solution evaluated from pressure history model[94] that is fitted using the data from Case "$0.5m/iz1/M$". The pressure is extracted near $r = r_m$.

ahead of the shock front for the smaller mass flow rate cases. These observations suggest that the averaged circumference introduces a geometrical constraint to the maximum fill height that can be supported by a given combustor. Pressure is adjusted to this constraint by maintaining similar $\bar{p}/\bar{p}_{pre}$ profiles when the mass flow rate exceeds 0.5m, although the pre-shock pressure increases with increasing mass flow rates, as shown in Fig. 18 (a). Note that no wave bifurcation is observed in these simulations even when the pre-shock pressure becomes extreme (e.g., $5 \sim 15$ bar), which shows that wave bifurcation does not necessarily result from increasing stagnation pressure or inlet mass flow rates; when no local hot spots or parasitic burning are present, as carefully designed and implemented in this study, one-wave mode can be sustained across a wide range of inlet conditions.

The smallest mass flow rate in this study is 0.06 kg/s (Case "$0.05m/iz1/M3$"), below which detonation cannot be sustained. At this condition, the fill height l_{cr} is approximately 8 mm (see Fig. 16(a)), and the wave speed is approximately 85% of the corresponding CJ velocity u_{cj} (see Fig. 16(b)). Figure 18(b) shows the pressure expansion distance dis_{exp}, which is defined as the distance where post-shock pressure falls to 0.5% of the pre-shock pressure. The hydrodynamic thickness h_t, which is measured between the shock front and the Ma = 0.995 location from the ZND solution, is also plotted. With decreasing mass flow rates, the pre-shock pressure drops, and the hydrodynamic thickness h_t increases. Interestingly, the expansion distance at the smallest mass flow rate corresponds to the hydrodynamic thickness at corresponding conditions. Further reduction of the mass flow rate would induce even smaller pre-shock pressure and larger hydrodynamic thickness h_t, while the fill height l_{cr} and pressure expansion distance dis_{exp} continue to drop. Consequently, the expansion distance dis_{exp} falls below h_t, which can be interpreted as a violation of the necessary choking condition to sustain detonation waves.

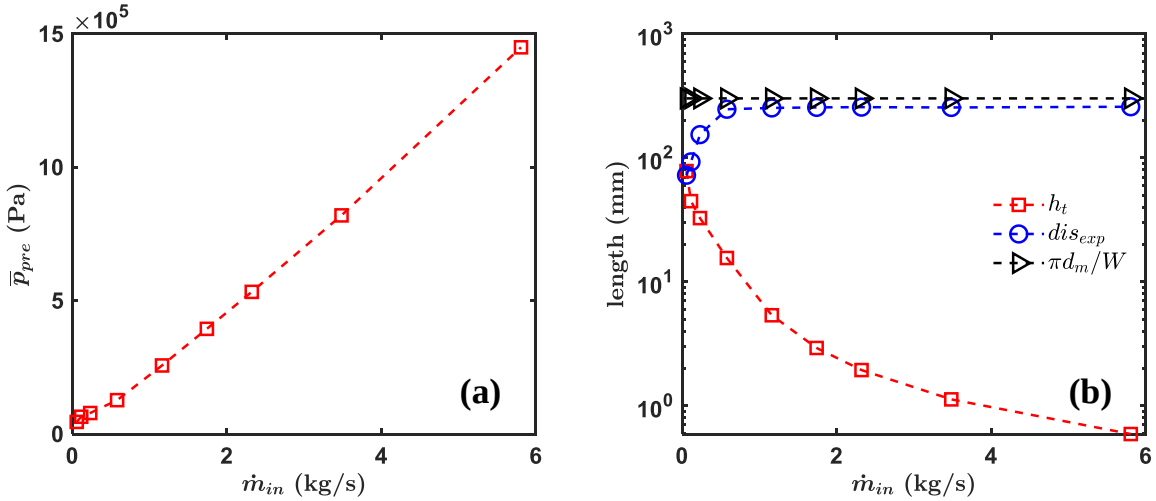

Figure 18: Variations of (a) mean pre-shock pressure and (b) expansion distance dis_{exp} near the inlet patch (the first-layer cell). The hydrodynamic thickness h_t and the circumferential distance per wave $\pi d_m/W$ (W is always 1) from the cases with different mass flow rate $\dot{m}_{in}$ are also plotted in (b). The pressure and dis_{exp} are extracted near $r = r_m$.

3.3.3. Effects of initiating multiple waves

Wave bifurcation in presence of multiple waves (equivalent to multiple initial hot spots) is investigated in this section through initiating multiple ignition regions that are evenly distributed, as shown in Fig. 19. All thermo-physical parameters are maintained identical for each ignition location, which corresponds to the mode-locked condition that is described in Ref. [95].

As an example, Fig. 19 shows the evolution of detonation waves in Case "$m/iz3/M3$", which is initialized with three evenly distributed ignition zones (see $t = 0$ ms). Three detonation fronts are formed (see $t = 0.05 \sim 0.21$ ms) and are sustained in the annular chamber (see $t = 1.9$ ms). The number of stable detonation waves is identical with the number of ignition regions. An obvious reduction in the fill height l_{cr} is observed when the number of waves increases. Similar observations are made for all other cases up to 24 ignition zones.

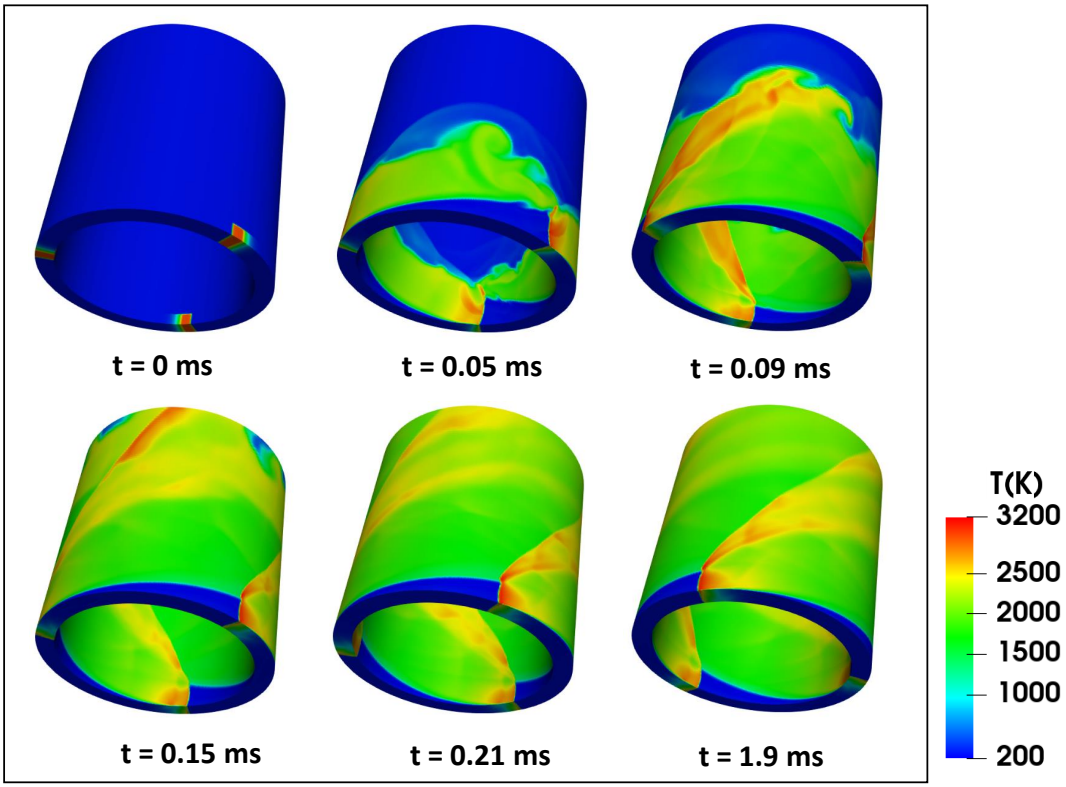

Figure 19: Snapshots of detonation waves obtained from Case "$m/iz3/M3$" at several time instants.

Figure 20(a) shows the fill height as a function of wave numbers. The fill height is inversely proportional to the number of waves. Simulations with 36 or 48 initial waves both fail to detonate, where deflagration combustion is advected downstream. Up to eight or nine waves have been reported in the literature [60, 57], where wave-wave interactions or deflagration to detonation transition (DDT) from local hot spots often contributes to wave bifurcation or coalition. The current study indicates that the presence of multiple existing waves in the system is not

a sufficient condition for wave-wave interactions and/or wave bifurcation, when waves are perfectly mode-locked and no additional stochastic hot spots are available. Figure 20(b) shows that the wave speed u_D almost drops linearly with increasing number of waves, while the CJ velocity u_{cj} is almost constant as there is little change in the pre-shock pressure p_{pre} as shown in Fig. 21(a). Decreasing wave speed has been reported when new waves are generated in experiments [95, 60, 57]. Intrinsically, variations of the velocity deficit $(u_{cj} - u_D)/u_{cj}$ as a function of wave number are caused by the lack of confinement on the top side of detonation wave. More analysis is shown in Sec. 3.3.4 to explain the observation.

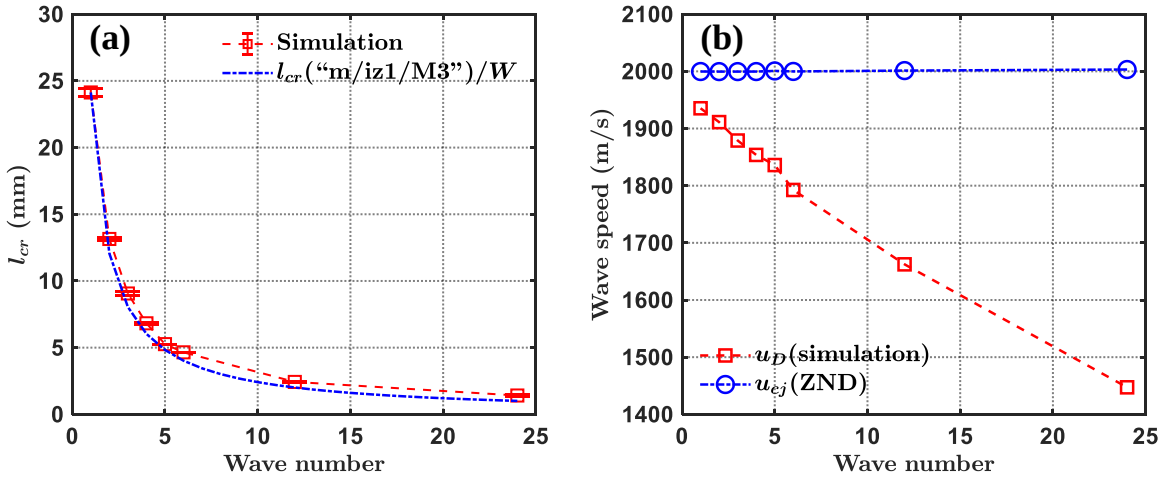

Figure 20: Variations of (a) the fill height l_{cr} and (b) detonation wave speed u_D as well as the CJ speed u_{cj} with wave number W. l_{cr}, u_{in} and p_{pre} used to calculate u_{CJ} are extracted near $r = r_m$.

The averaged pre-shock pressures p_{pre} and pressure expansion distance dis_{exp} are plotted in Fig. 21. It can been seen that the pre-shock pressure slightly increases with increasing number of waves. For the 24 waves case, the pressure expansion distance is approximately twice the hydrodynamic thickness, and the distance between two neighboring waves is approximately three times the hydrodynamic thickness. It is expected that the pressure expansion distance is further reduced to be close to the hydrodynamic thickness with 36 waves, which eventually leads to failure.

3.3.4. Velocity deficit

In addition to viscous and heat loss, the lack of confinement on the top side of the traveling waves is a third mechanism leading to a velocity deficit in rotating detonation combustors [95]. The loss from pressure expansion in RDCs can be explained by a pioneer study by Fay [96], where the effect of boundary layer on gaseous detonations in solids tubes was studied. Suppose the shock-front area of each streamtube is A_1 and the CJ-plane (or sonic-plane) area is A_2, the average fractional change in the area of each stream tube ξ is given by $(A_2/A_1 - 1)$, which can be employed to represent the expansion loss. By considering a 2D channel of width b bounded by inert gases on one side normal to b, Dabora et al. [97] showed that $\xi = (\overline{x} \cdot \tan\delta)/b$ where

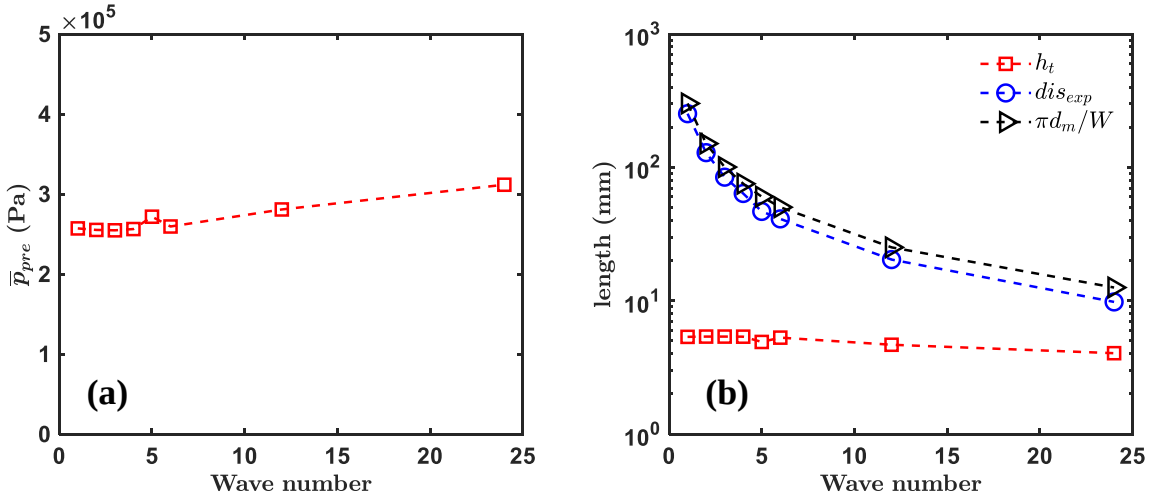

Figure 21: Variations of (a) mean pre-shock pressure and (b) expansion distance dis_{exp} near the inlet patch (the first-layer cell). The hydrodynamic thickness h_t and the circumferential distance per wave $\pi d_m/W$ from the cases with different wave numbers W are also plotted in (b). The pressure and dis_{exp} are extracted near $r = r_m$.

δ is the deflection angle of the interface between the inert layer and hot product and $\overline{x}$ is the reaction length separating the CJ plane from the shock front. For a given fresh mixture, a larger velocity deficit is observed in the experiments when b is thinner and ξ is larger. Similar trends are also captured in the recent 2D simulations [98, 99]. Following their analysis and replacing $\overline{x}$ and b by h_t and l_{cr}, respectively, the fractional area increase ξ for the current RDC is defined as

$$\xi = \frac{h_t \cdot (\tan\delta - \tan\alpha)}{l_{cr}} \ , \tag{13}$$

where the deflection of contact surface $(h_t \cdot \tan\alpha)$ is subtracted from the deflection of the flow. Figure 22 shows the variations of velocity deficit $(u_{cj} - u_D)/u_{cj}$ with fractional area increase $[h_t \cdot (\tan\delta - \tan\alpha)]/l_{cr}$ from the cases with different inlet mass flow rate $\dot{m}_{in}$ and wave numbers W. For both cases, the velocity deficit is positively correlated with the fractional area. Figure 23 compares the fractions of h_t/l_{cr}, $(\tan\delta - \tan\alpha)$ and $[h_t \cdot (\tan\delta - \tan\alpha)]/l_{cr}$ from all cases. It can be seen that the change in $[h_t \cdot (\tan\delta - \tan\alpha)]/l_{cr}$ is mainly contributed by the variation of h_t/l_{cr}, as the change in $(\tan\delta - \tan\alpha)$ is relatively insignificant compared to h_t/l_{cr}.

When the mass flow rate is decreased, h_t becomes longer with decreasing pre-shock pressure, l_{cr} becomes shorter, and hence h_t/l_{cr} gets larger. When wave number is increased, h_t is almost fixed (see Fig. 21(b)), because p_{pre} barely changes as shown in Fig. 21(a). l_{cr} decreases with wave number W (see Fig. 20(a)), therefore, h_t/l_{cr} increases with W. In this study, we observed that detonation quenches when the pressure expansion distance is comparable to the hydrodynamic thickness. From a physical point of view, when the velocity deficit increases to certain point, the shock strength drops so much that the post-shock temperature and pressure cannot ignite the mixture within a reasonable amount of time, which eventually leads to failure.

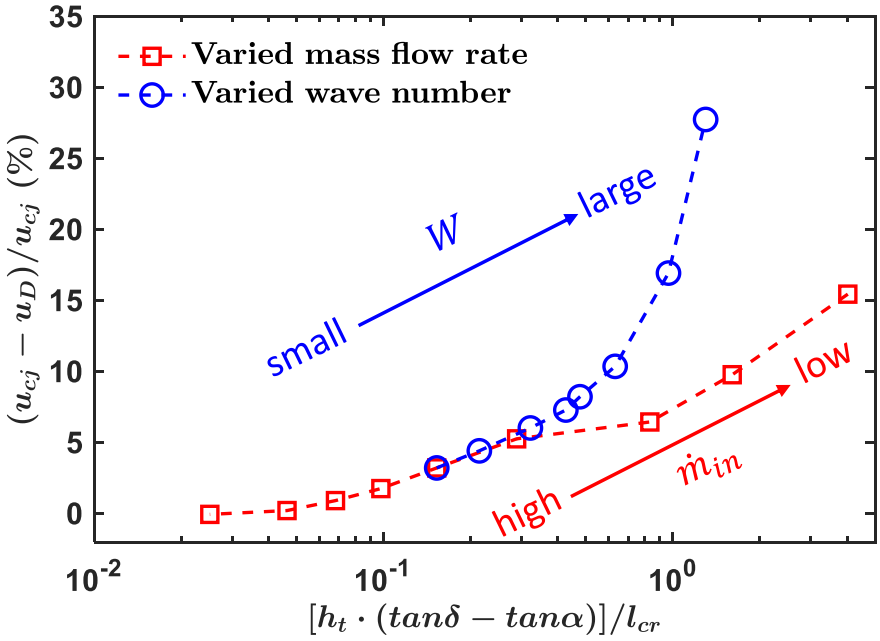

Figure 22: Variations of velocity deficit $(u_{cj} - u_D)/u_{cj}$ with fractional area increase $[h_t \cdot (tan\delta - tan\alpha)]/l_{cr}$ from the cases with different inlet mass flow rate $\dot{m}_{in}$ and wave numbers W. u_D, $tan\delta$ and l_{cr} are extracted near $r = r_m$.

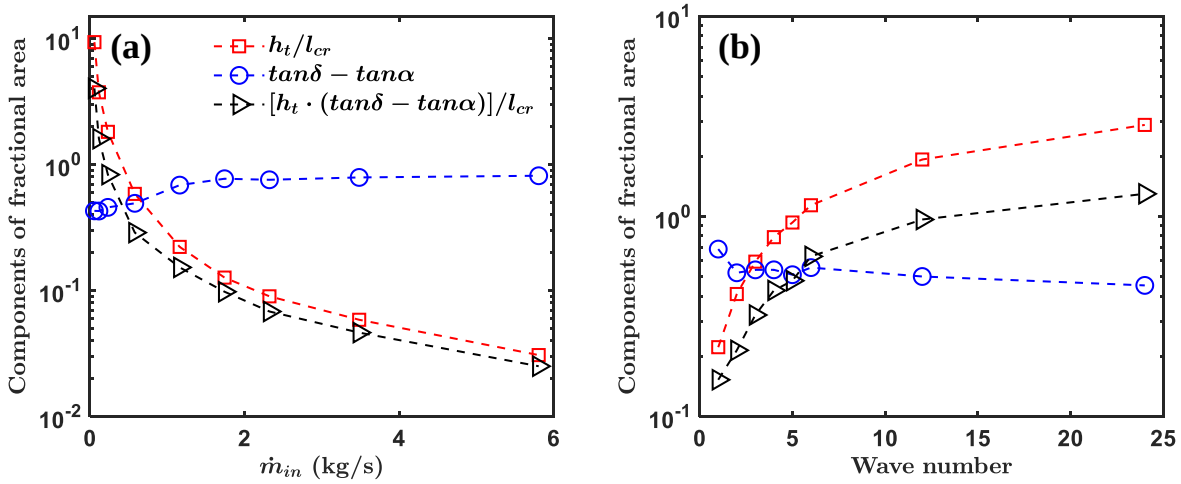

Figure 23: Variations of h_t/l_{cr}, $(\tan\delta - \tan\alpha)$ and $[h_t \cdot (\tan\delta - \tan\alpha)]/l_{cr}$ with different (a) inlet mass flow rates $\dot{m}_{in}$ and (b) wave numbers W.

3.3.5. Discussions of the predictability of fill height and wave number

Results in Sec. 3.3.2 demonstrate that large mass flow rate is not a sufficient condition for wave bifurcation. Furthermore, results in Sec. 3.3.3 show that presence of multiple waves is

also not a sufficient condition for wave bifurcation. In addition, the number of waves cannot be uniquely determined simply based on the inlet boundary condition and the combustor geometry, because the number of initiation locations, or stochastic hot spots, can determine the number of waves present in a combustor. In either case, the fill height and wave number are closely related with the pressure expansion process along the azimuthal direction of the combustor, which seems to play a significant role here.

Attempt has been made in the literature to theoretically to predict the stability of detonation front and detonation wave number W [64, 65]. For example, Eq. 14 from Ref. [65] predicts the wave number W by comparing the time scale of one revolution t_r to the time scale of consuming the fresh mixture ahead of the detonation wave t_{mf},

$$W = \frac{t_r}{t_{mf}} = \frac{\dot{V}_{mix}}{V_{cr}/t_r} = \frac{\dot{V}_{mix}}{\dot{V}_{consume}} \ . \tag{14}$$

Here $t_r = \pi d_m/u_D$, and the detonation velocity u_D is also evaluated at the averaged diameter location. The critical volume V_{cr} is calculated through

$$V_{cr} = \pi/4(d_o^2 - d_i^2)l_{cr} \ , \tag{15}$$

where V_{cr} indicates the consumed volume that is swept by the detonation wave within one revolution. The volumetric supply rate of the fresh mixture can be computed as

$$\dot{V}_{mix} = \dot{m}_{in}/\rho_{mix} \ . \tag{16}$$

The detonation wave number W equal to 1, 2, 3 or n suggests that there are 1, 2, 3 or n detonation heads propagating in one direction in the combustor. Re-arranging Eq. 14, we obtain Eq. 17, which essentially states that the number of detonation waves is determined by the ratio of the inlet mass flow rate $\dot{m}_{in}$ and the mass consumption rate by each detonation wave $\rho_{mix}(u_D h l_{cr})$.

$$W = \frac{\dot{m}_{in}/\rho_{mix}}{[\pi/4(d_o^2 - d_i^2)l_{cr}/(\pi d/u_D)]} = \frac{\dot{m}_{in}}{\rho_{mix}(u_D h l_{cr})} \ . \tag{17}$$

Further re-arranging Eq. 17 and substituting $\dot{m}_{in}$ by $\rho_{mix}u_{in}A_{in}$, l_{cr} can be expressed by

$$\frac{l_{cr}}{\pi d_m/W} = \frac{u_{in}}{u_D} \ , \tag{18}$$

where $d_m = (d_o + d_i)/2$. Equation 18 shows that the fill height l_{cr} scales with the average circumference πd_m divided by the number of waves W. Consistent with the observations in previous sections, $\pi d_m/W$ is the maximum azimuthal expansion distance for each wave. The non-dimensionalized l_{cr} is determined by the velocity ratio u_{in}/u_D. The proportionality between l_{cr} and d_m has been discussed in previous 2D simulations [100]. This equation quantitatively explains the change of the fill height due to varied u_{in} and d_m predicted by a fast 2D model developed by Sousa et al. [101] based on mass conservation.

Figure 24 shows the left-hand side versus the right-hand side of Eq. 18 using all the simulations data in this study. A linear relation is observed, which is a natural result of mass

conservation in all the simulations. However, Eqs. 17 or 18 cannot be expected to "predict" the number of waves in a specific RDC, given specified operating conditions. To "predict" wave numbers, it is important to accurately account for all the deterministic and stochastic events that can lead to wave bifurcation, e.g., local hot spots and DDT, etc. Therefore, it would be more meaningful to study the limit conditions and critical physico-chemical conditions that lead to those, rather than predicting the exact number of waves in a system. Results from the current study attempt to provide the upper and lower limits of l_{cr} when increasing mass flow rates and increasing wave initiations, under the assumptions of reactive Euler governing equations, perfectly mode-locked initial conditions, perfectly premixed inlet boundary conditions, and constant inlet mass flux. In addition, the various lengths and velocities are measured based on certain arbitrarily chosen thresholds. Therefore, the criteria of the lower and upper limit conditions in this study should be interpreted as an order of magnitude indication. Future studies will focus on exploring these limit conditions while considering viscous effects and inhomogeneous mixtures where more stringent resolution requirements apply [102, 103].

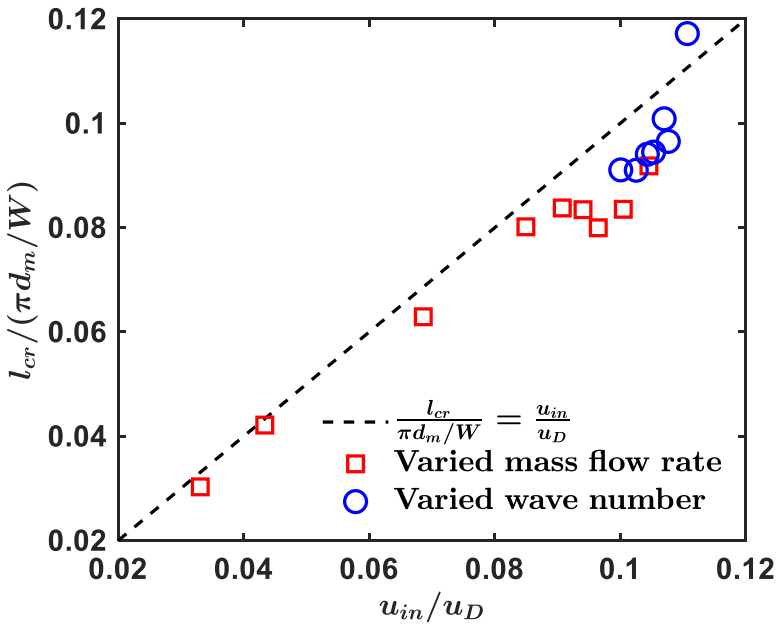

Figure 24: Variations of u_{in}/u_D and $l_{cr}/(\pi d_m/W)$ from the cases with different inlet mass flow rate $\dot{m}_{in}$ and wave numbers W. u_{in}, u_D and l_{cr} are extracted near $r = r_m$. The simulation data tend to under-predict the fill height l_{cr}, due to the arbitrarily chosen threshold used in defining l_{cr}.

3.4. Summary

Numerical simulations of a three-dimensional model RDC are conducted using a recently developed compressible reacting flow solver to study mechanisms of wave bifurcation. The solver has been verified using 1D hydrogen/oxygen/argon detonation and a 2D hydrogen/air configuration, where the detonation wave speed is well captured by a large range of grid resolutions. Subsequently, the wave dynamics in a model RDC with premixed hydrogen/air is studied. An

ideal injection system with a fixed mass flow rate boundary condition is proposed to avoid complexities that arise from complex injector dynamics. Influences of grid resolutions, inflow mass flow rate and initiations of ignition spots are investigated and main findings are summarized below.

The first-level cell height near the inlet surface should be sufficiently refined, because it directly controls the mixing between hot products and the fresh mixture. Large cell height increases the cell-centered temperature near the inlet, which can serve as an igniter to numerically introduce multiple waves. One detonation wave is maintained throughout the simulation once the mesh is sufficiently refined in the streamwise direction.

As inflow mass flow rate increases, the peak pressure of the detonation wave becomes proportionally higher. The dynamics of fill height seems to be controlled by the coupling between the internal pressure field and the inlet boundary condition. The circumference of the combustor constrains the maximum expansion distance for the post-shock pressure, and a maximum value of fill height is achieved when the downstream outlet boundary condition becomes supersonic. Increasing mass flow rates beyond this point does not lead to wave bifurcation or further increase of the fill height, although the fluctuation of the fill height seems to grow with extreme mass flow rates. The minimal fill height observed in these numerical experiments corresponds to the smallest mass flow rate at which the pressure expansion distance is approximately the same as the hydrodynamic thickness that is defined based on ZND solutions.

The number of waves is not uniquely determined by the inlet boundary conditions; multiple initial ignition regions can lead to multiple stably rotating waves. Consequently, the fill height cannot be solely determined based on the inlet condition, as it is closely related to the number of existing waves in the combustor. The existence of multiple waves is also not a sufficient condition for wave-wave interactions or wave bifurcation; they can stably co-exist in a mode-locked manner when no hot spots or disturbance exist. The maximum number of waves, hence the minimum fill height, are again constrained by the pressure expansion distance, which is measured to be approximately two hydrodynamic thickness for 24 waves.

Either lower mass flow rates or larger wave numbers can increase the velocity deficit, which results from lack of confinement on the top side of the traveling waves in rotating detonation combustors. The concept of a fractional area increase of the the CJ (or sonic) plane compared with the area of the shock front is employed to explain the loss. For both cases, the ratio of the hydrodynamic distance and fill height is the critical parameter that determines the level of velocity deficit.

A mass-conservation based interpretation of Wolański's formula [64, 65] is derived, where the fill height scales with the circumference divided by the wave number, and can be determined by the ratio of inlet velocity and wave speed. Data from the simulations show consistency with this relation, simply indicating that all the fuel has been converted to products within the combustor. Synthesizing all the results in this study and those observed in the literature, it is shown that it is unlikely that the number of waves, hence the fill height, can be "predicted" based on the inlet condition and the geometry alone; other factors, such as stochastic local hot spots, can lead to wave bifurcation. Future studies will focus on understanding the limit conditions for the fill height when more realistic physics is considered, including the detailed detonation structure, the viscous effects and heat loss through walls.

References

[1] J. H. Chen, "Petascale direct numerical simulation of turbulent combustion—fundamental insights towards predictive models," *Proceedings of Combustion Institute*, vol. 33, pp. 99–123, 2011.

[2] J. M. Stone, T. A. Gardiner, P. Teuben, J. F. Hawley, and J. B. Simon, "Athena: a new code for astrophysical mhd," *Astrophysical Journal Supplement Series*, vol. 178, p. 137, 2008.

[3] "Dynamic load balancing." https://github.com/OpenFOAM/OpenFOAM-dev, 2022.

[4] A. Krisman, P. Meagher, X. Zhao, J.-W. Park, T. Lu, and J. H. Chen, "A direct numerical simulation of jet a flame kernel quenching," *Combustion and Flame*, vol. 225, p. 349–363, Mar. 2021.

[5] P. A. Meagher, S. C. III, J.-W. Park, and X. Zhao, "Responses of turbulent methane/air kernels to perturbed chemical kinetic models," *Combustion and Flame*, in preparation.

[6] P. A. Meagher, A. S. Jayaraman, N. Kateris, X. Shi, X. Zhao, M. Radulescu, A. Kempf, A. Y. Poludnenko, and H. Wang, "Detonation cells arise from microscopic jetting," *Physical Review Letters*, Under review.

[7] P. Zhang, P. A. Meagher, and X. Zhao, "Multiplicity for idealized rotational detonation waves," *Physics of Fluids*, vol. 33, Oct. 2021.

[8] P. A. Meagher, S. C. III, J.-W. Park, and X. Zhao, "Effect of laminar flame properties on the global response of flames subject to extreme turbulence," in *18th International Confrence on Numerical Combustion*, 8–11 May 2022.

[9] P. A. Meagher and X. Zhao, "Direct numerical simulation of a turbulent premixed flame kernel," in *2020 Spring Technical Meeting of the Eastern States Section of the Combustion Institute*, 8–11 March 2020.

[10] P. A. Meagher, S. S. Dammati, X. Zhao, A. Y. Poludnenko, X. Shi, J. Crane, and H. Wang, "Effects of grid resolution and boundary conditions on 2d simuations of single headed hydrogen detonations," in *12th United States National Combustion Meeting*, 25–26 May 2021.

[11] P. A. Meagher, X. Shi, J. Crane, S. S. Dammati, X. Zhao, A. Y. Poludnenko, and H. Wang, "Gas phase detonation fundamentals: Microscopic jetting as the origin of the detonation cell cycle," in *National Rotating Detonation Engine Council Meeting*, 12–14 July 2022.

[12] P. A. Meagher, X. Shi, J. Crane, X. Zhao, S. S. Dammati, A. Y. Poludnenko, and H. Wang, "Cell structure and global heat release in 2D and 3D JP10-air detonations in narrow channels," in *Proceedings of the 28th ICDERS* [104].

[13] P. A. Meagher, X. Shi, J. Crane, X. Zhao, S. S. Dammati, A. Y. Poludnenko, and H. Wang, "Forward jetting phenomenon in detonations," in *Proceedings of the 28th ICDERS* [104].

[14] P. A. Meagher, S. S. Dammati, X. Shi, J. Crane, A. Y. Poludnenko, H. Wang, and X. Zhao, "Towards a hydrogen detonation combustor: using high-fidelity simulation to quantify wall losses for hydrogen-oxygen and hydrogen-air detonations in narrow ducts," in *C2E2 Clean Energy Symposium*, 19–20 May 2022.

[15] P. A. Meagher, X. Shi, J. P. Santos, N. K. Muraleedharan, J. Crane, A. Y. Poludnenko, H. Wang, and X. Zhao, "Isolating gasdynamic and chemical effects on the detonation cellular structure: A combined experimental and computational study," *Proceedings of the Combustion Institute*, vol. 39, no. 3, p. 2865–2873, 2023.

[16] P. A. Meagher, X. Shi, A. S. Jayaraman, N. Kateris, X. Zhao, and H. Wang, "Microscopic fluid jetting as the origin of the detonation cell," in *13th United States National Combustion Meeting*, 19–22 March 2023.

[17] P. A. Meagher, X. Shi, A. S. Jayaraman, N. Kateris, X. Zhao, and H. Wang, "The hydrodynamic origin of the detonation cell," in *Proceedings of the 29th ICDERS*, Institute for Dynamics of Explosions and Reactive Systems, 2023.

[18] X. Shi, P. A. Meagher, J. Crane, S. S. Dammati, X. Zhao, A. Y. Poludnenko, and H. Wang, "On cellular multiplicity of detonation in confined channels," in *Proceedings of the 28th ICDERS* [104].

[19] X. Shi, P. A. Meagher, J. P. Santos, N. K. Muraleedharan, J. Crane, A. Y. Poludnenko, X. Zhao, and H. Wang, "Isolating gasdynamic and chemical effects on detonation cellular structure and regularity," in *2022 Spring Hybrid Meeting of the Western States Section of the Combustion Institute*, 21–22 May 2022.

[20] A. Krisman, P. Meagher, X. Zhao, J.-W. Park, T. Lu, and J. Chen., "The interaction of high-speed turbulence with flames: Global properties and internal flame structure," *Combustion and Flame*, vol. 157, no. 5, pp. 995 – 1011, 2010.

[21] G. Smith, Y. Tao, and H. Wang, "Foundational fuel chemistry model version 1.0 (FFCM-1)." http://nanoenergy.stanford.edu/ffcm1, 2016.

[22] D. Baulch, C. Bowman, C. Cobos, R. Cox, T. Just, J. Kerr, M. Pilling, D. Stocker, J. Troe, W. Tsang, and R. Walker, "Evaluated kinetic data for combustion modeling: supplement II," *Journal of Physical and Chemical Reference Data*, vol. 34, pp. 757–1397, 2005.

[23] D. G. Goodwin, R. L. Speth, H. K. Moffat, and B. W. Weber, "Cantera: An object-oriented software toolkit for chemical kinetics, thermodynamics, and transport processes." https://www.cantera.org, 2018. Version 2.4.0.

[24] C. Rosales and C. Meneveau, "Linear forcing in numerical simulations of isotropic turbulence: Physical space implementations and convergence properties," *Physics of Fluids*, vol. 17, no. 9, p. 095106, 2005.

[25] J. H. Chen, A. Choudhary, B. D. Supinski, M. DeVries, E. R. Hawkes, S. Klasky, W. K. Liao, K. L. Ma, J. Mellor-Crummey, N. Podhorszki, R. Sankaran, S. Shende, and C. S.

Yoo, "Terascale direct numerical simulations of turbulent combustion using S3D," *Computational Science and Discovery*, vol. 2, p. 015001, jan 2009.

[26] D. Bradley, M. Shehata, M. Lawes, and P. Ahmed, "Flame extinctions: Critical stretch rates and sizes," *Combustion and Flame*, vol. 212, pp. 459–468, 2020.

[27] E. R. Hawkes and J. H. Chen, "Comparison of direct numerical simulation of lean premixed methane–air flames with strained laminar flame calculations," *Combustion and Flame*, vol. 144, no. 1, pp. 112–125, 2006.

[28] R. A. Strehlow and A. J. Crooker, "The structure of marginal detonation waves," *Acta Astronautica*, vol. 1, no. 3-4, pp. 303–315, 1974.

[29] R. Takai, K. Yoneda, and T. Hikita, "Study of detonation wave structure," *Symposium (Int.) on Combustion*, vol. 15, no. 1, pp. 69–78, 1975.

[30] A. A. Vasiliev and Y. Nikolaev, "Closed theoretical model of a detonation cell," *Acta Astronautica*, vol. 5, no. 11-12, pp. 983–996, 1978.

[31] A. A. Vasil'ev, "Cell size as the main geometric parameter of a multifront detonation wave," *Journal of Propulsion and Power*, vol. 22, no. 6, pp. 1245–1260, 2006.

[32] J. Crane, X. Shi, J. T. Lipkowicz, A. M. Kempf, and H. Wang, "Geometric modeling and analysis of detonation cellular stability," *Proceedings of Combustion Institute*, vol. 38, pp. 3585–3593, 2021.

[33] V. A. Subbotin, "Collision of transverse detonation waves in gases," *Combustion, Explosion and Shock Waves*, vol. 11, no. 3, pp. 411–414, 1975.

[34] L. Massa, J. M. Austin, and T. Jackson, "Triple-point shear layers in gaseous detonation waves," *Journal of Fluid Mechanics*, vol. 586, pp. 205–248, 2007.

[35] M. I. Radulescu, G. J. Sharpe, C. K. Law, and J. H. Lee, "The hydrodynamic structure of unstable cellular detonations," *Journal of Fluid Mechanics*, vol. 580, pp. 31–81, 2007.

[36] C. B. Kiyanda and A. J. Higgins, "Photographic investigation into the mechanism of combustion in irregular detonation waves," *Shock Waves*, vol. 23, no. 2, pp. 115–130, 2013.

[37] E. A. Lundstrom and A. K. Oppenheim, "On the influence of non-steadiness on the thickness of the detonation wave," *Proceedings of the Royal Society of London. A. Mathematical and Physical Sciences*, vol. 310, no. 1503, pp. 463–478, 1969.

[38] J. Austin, F. Pintgen, and J. Shepherd, "Lead shock oscillation and decoupling in propagating detonations," in *43rd AIAA Aerospace Sciences Meeting and Exhibit*, p. 1170, 2005.

[39] F. Pintgen, C. A. Eckett, J. M. Austin, and J. E. Shepherd, "Direct observations of reaction zone structure in propagating detonations," *Combustion and Flame*, vol. 133, no. 3, pp. 211–229, 2003.

[40] J. M. Austin, F. Pintgen, and J. E. Shepherd, "Reaction zones in highly unstable detonations," *Proceedings of the Combustion Institute*, vol. 30, no. 2, pp. 1849–1857, 2005.

[41] H. Hornung, "Regular and mach reflection of shock waves," *Annual Review of Fluid Mechanics*, vol. 18, no. 1, pp. 33–58, 1986.

[42] L. F. Henderson, E. I. Vasilev, G. Ben-Dor, and T. Elperin, "The wall-jetting effect in mach reflection: theoretical consideration and numerical investigation," *Journal of Fluid Mechanics*, vol. 479, pp. 259–286, 2003.

[43] E. I. Vasilev, G. Ben-Dor, T. Elperin, and L. F. Henderson, "The wall-jetting effect in mach reflection: Navier–stokes simulations," *Journal of Fluid Mechanics*, vol. 511, pp. 363–379, 2004.

[44] R. R. Bhattacharjee, S. S. M. Lau-Chapdelaine, G. Maines, L. Maley, and M. I. Radulescu, "Detonation re-initiation mechanism following the mach reflection of a quenched detonation," *Proceedings of the Combustion Institute*, vol. 34, no. 2, pp. 1893–1901, 2013.

[45] S. S.-M. Lau-Chapdelaine, Q. Xiao, and M. I. Radulescu, "Viscous jetting and mach stem bifurcation in shock reflections: experiments and simulations," *Journal of Fluid Mechanics*, vol. 908, 2021.

[46] M. I. Radulescu, A. Papi, J. J. Quirk, P. Mach, and B. M. Maxwell, "The origin of shock bifurcations in cellular detonations," in *22nd International Colloquium on the Dynamics of Explosions and Reactive Systems*, p. 4, 2009.

[47] P. Mach and M. I. Radulescu, "Mach reflection bifurcations as a mechanism of cell multiplication in gaseous detonations," *Proceedings of the Combustion Institute*, vol. 33, no. 2, pp. 2279–2285, 2011.

[48] L. Maley, R. Bhattacharjee, S.-M. Lau-Chapdelaine, and M. I. Radulescu, "Influence of hydrodynamic instabilities on the propagation mechanism of fast flames," *Proceedings of the Combustion Institute*, vol. 35, no. 2, pp. 2117–2126, 2015.

[49] G. Ciccarelli and S. Dorofeev, "Flame acceleration and transition to detonation in ducts," *Progress in Energy and Combustion Science*, vol. 34, no. 4, pp. 499–550, 2008.

[50] P. A. Meagher, X. Shi, J. P. Santos, N. K. Muraleedharan, J. Crane, A. Y. Poludnenko, H. Wang, and X. Zhao, "Isolating gasdynamic and chemical effects on the detonation cellular structure: A combined experimental and computational study," *Proceedings of the Combustion Institute, in press*, 2022.

[51] J. H. Lee, *The detonation phenomenon*. 2008.

[52] X. Hu, D. Zhang, and Z. Jiang, "Analytical study of idealized two-dimensional cellular detonations," *Shock Waves*, vol. 11, no. 6, pp. 475–480, 2002.

[53] S. S.-M. Lau-Chapdelaine, Q. Xiao, and M. I. Radulescu, "Viscous jetting and mach stem bifurcation in shock reflections: experiments and simulations," *Journal of Fluid Mechanics*, vol. 908, 2020.

[54] A. Sow, S.-M. Lau-Chapdelaine, and M. I. Radulescu, "The effect of the polytropic index γ on the structure of gaseous detonations," *Proceedings of the Combustion Institute*, vol. 38, no. 3, pp. 3633–3640, 2021.

[55] B. A. Rankin, D. R. Richardson, A. W. Caswell, A. G. Naples, J. L. Hoke, and F. R. Schauer, "Chemiluminescence imaging of an optically accessible non-premixed rotating detonation engine," *Combustion and Flame*, vol. 176, 2017.

[56] F. A. Bykovskii, S. A. Zhdan, and E. F. Vedernikov, "Continuous spin detonations," *Journal of Propulsion and Power*, vol. 22, pp. 1204–1216, 2006.

[57] F. A. Bykovskii, S. A. Zhdan, and E. F. Vedernikov, "Continuous spin detonation in annular combustors," *Combustion, Explosion, and Shock Waves*, vol. 41, pp. 449–459, 2005.

[58] J. Suchocki, S.-T. Yu, J. Hoke, A. Naples, F. Schauer, and R. Russo, "Rotating detonation engine operation," *50th AIAA Aerospace Sciences Meeting Including the New Horizons Forum and Aerospace Exposition*, p. 119, 2012.

[59] V. Anand, A. S. George, R. Driscoll, and E. Gutmark, "Investigation of rotating detonation combustor operation with H_2-air mixtures," *International Journal of Hydrogen Energy*, vol. 41, pp. 1281–1292, 2016.

[60] D. P. Stechmann, S. D. Heister, and S. V. Sardeshmukh, "High-pressure rotating detonation engine testing and flameholding analysis with hydrogen and natural gas," *55th AIAA Aerospace Sciences Meeting*, p. 1931, 2017.

[61] A. S. George, R. Driscoll, V. Anand, and E. Gutmark, "On the existence and multiplicity of rotating detonations," *Proceedings of Combustion Institute*, vol. 36, pp. 2691–2698, 2017.

[62] B. A. Rankin, J. R. Codoni, K. Y. Cho, J. L. Hoke, and F. R. Schauer, "Investigation of the structure of detonation waves in a non-premixed hydrogen–air rotating detonation engine using mid-infrared imaging," *Proceedings of Combustion Institute*, vol. 37, pp. 3479–3486, 2019.

[63] F. K. Lu and E. M. Braun, "Rotating detonation wave propulsion: experimental challenges, modeling, and engine concepts," *Journal of Propulsion and Power*, vol. 30, pp. 1125–1142, 2014.

[64] P. Wolański, "Rotating detonation wave stability," *23rd International Colloquium on the Dynamics of Explosions and Reactive Systems*, pp. 1–6, 2011.

[65] P. Wolański, "Detonative propulsion," *Proceedings of Combustion Institute*, vol. 34, pp. 125–158, 2013.

[66] S.-J. Liu, Z.-Y. Lin, W.-D. Liu, W. Lin, and F.-C. Zhuang, "Experimental realization of H_2/air continuous rotating detonation in a cylindrical combustor," *Combustion Science and Technology*, vol. 184, pp. 1302–1317, 2012.

[67] S. Frolov, V. Aksenov, V. Ivanov, and I. Shamshin, "Large-scale hydrogen-air continuous detonation combustor," *International Journal of Hydrogen Energy*, vol. 40, pp. 1616–1623, 2015.

[68] W. Lin, J. Zhou, S. Liu, Z. Lin, and F. Zhuang, "Experimental study on propagation mode of H_2/air continuously rotating detonation wave," *International Journal of Hydrogen Energy*, vol. 40, pp. 1980–1993, 2015.

[69] V. Anand and E. Gutmark, "Rotating detonation combustors and their similarities to rocket instabilities," *Progress in Energy and Combustion Science*, vol. 73, pp. 182–234, 2019.

[70] D. Schwer and K. Kailasanath, "Feedback into mixture plenums in rotating detonation engines," *50th AIAA Aerospace Sciences Meeting Including the New Horizons Forum and Aerospace Exposition*, p. 617, 2012.

[71] S. Yao, M. Liu, and J. Wang, "Numerical investigation of spontaneous formation of multiple detonation wave fronts in rotating detonation engine," *Combustion Science and Technology*, vol. 187, pp. 1867–1878, 2015.

[72] S. Yao and J. Wang, "Multiple ignitions and the stability of rotating detonation waves," *Applied Thermal Engineering*, vol. 108, pp. 927–936, 2016.

[73] J. Sun, J. Zhou, S. Liu, Z. Lin, and J. Cai, "Effects of injection nozzle exit width on rotating detonation engine," *Acta Astronaut.*, vol. 140, pp. 388–401, 2017.

[74] S. M. Frolov, V. S. Aksenov, V. S. Ivanov, S. N. Medvedev, and I. O. Shamshin, "Flow structure in rotating detonation engine with separate supply of fuel and oxidizer: experiment and CFD," *Detonation Control for Propulsion, Springer*, pp. 39–59, 2018.

[75] Y. Liu, W. Zhou, Y. Yang, Z. Liu, and J. Wang, "Numerical study on the instabilities in H_2-air rotating detonation engines," *Physics of Fluids*, vol. 30, p. 046106, 2018.

[76] L. Deng, H. Ma, C. Xu, X. Liu, and C. Zhou, "The feasibility of mode control in rotating detonation engine," *Applied Thermal Engineering*, vol. 129, pp. 1538–1550, 2018.

[77] J. Koch and J. N. Kutz, "Modeling thermodynamic trends of rotating detonation engines," *Physics of Fluids*, vol. 32, p. 126102, 2020.

[78] M. Zhao and H. Zhang, "Origin and chaotic propagation of multiple rotating detonation waves in hydrogen/air mixtures," *Fuel*, vol. 275, p. 117986, 2020.

[79] W. Chen, J. Liang, X. Cai, and Y. Mahmoudi, "Three-dimensional simulations of detonation propagation in circular tubes: effects of jet initiation and wall reflection," *Physics of Fluids*, vol. 32, p. 046104, 2020.

[80] M. Zhao, M. J. Cleary, and H. Zhang, "Combustion mode and wave multiplicity in rotating detonative combustion with separate reactant injection," *Combustion and Flame*, vol. 225, pp. 291–304, 2021.

[81] C. Lietz, M. Ross, Y. Desai, and W. A. Hargus, "Numerical investigation of operational performance in a methane-oxygen rotating detonation rocket engine," *AIAA Scitech 2020 Forum*, p. 0687, 2020.

[82] C. Li, K. Kailasanath, and G. Patnaik, "A numerical study of flow field evolution in a pulsed detonation engine," *38th Aerospace Sciences Meeting and Exhibit*, p. 314, 2000.

[83] D. Schwer and K. Kailasanath, "Numerical investigation of rotating detonation engines," *46th AIAA/ASME/SAE/ASEE Joint Propulsion Conference & Exhibit*, p. 6880, 2010.

[84] J.-Y. Choi, I.-S. Jeung, and Y. Yoon, "Computational fluid dynamics algorithms for unsteady shock-induced combustion, part 1: validation," *AIAA Journal*, vol. 38, pp. 1179–1187, 2000.

[85] C. J. Greenshields, H. G. Weller, L. Gasparini, and J. M. Reese, "Implementation of semi-discrete, non-staggered central schemes in a colocated, polyhedral, finite volume framework, for high-speed viscous flows," *International Journal for Numerical Methods in Fluids*, vol. 63, pp. 1–21, 2010.

[86] B. Wu, X. Zhao, B. R. Chowdhury, B. M. Cetegen, C. Xu, and T. Lu, "A numerical investigation of the flame structure and blowoff characteristics of a bluff-body stabilized turbulent premixed flame," *Combustion and Flame*, vol. 202, pp. 376–393, 2019.

[87] C. White, M. K. Borg, T. J. Scanlon, S. M. Longshaw, B. John, D. R. Emerson, and J. M. Reese, "dsmcfoam+: An openfoam based direct simulation monte carlo solver," *Computer Physics Communications*, vol. 224, pp. 22–43, 2018.

[88] D. A. Schwer, R. F. Johnson, A. Kercher, D. A. Kessler, and A. T. Corrigan, "Numerical investigation of centerbody-less rotating detonation combustors," *AIAA Scitech 2020 Forum*, p. 2158, 2020.

[89] D. Schwer and K. Kailasanath, "Numerical investigation of the physics of rotating-detonation-engines," *Proceedings of Combustion Institute*, vol. 33, pp. 2195–2202, 2011.

[90] D. Schwer and K. Kailasanath, "Fluid dynamics of rotating detonation engines with hydrogen and hydrocarbon fuels," *Proceedings of Combustion Institute*, vol. 34, pp. 1991–1998, 2013.

[91] N. Tsuboi, S. Eto, A. K. Hayashi, and T. Kojima, "Front cellular structure and thrust performance on hydrogen–oxygen rotating detonation engine," *Journal of Propulsion and Power*, vol. 33, pp. 100–111, 2017.

[92] V. R. Katta, K. Y. Cho, J. L. Hoke, J. R. Codoni, F. R. Schauer, and W. M. Roquemore, "Effect of increasing channel width on the structure of rotating detonation wave," *Proceedings of Combustion Institute*, vol. 37, pp. 3575–3583, 2019.

[93] T. Sato, F. Chacon, L. White, V. Raman, and M. Gamba, "Mixing and detonation structure in a rotating detonation engine with an axial air inlet," *Proceedings of Combustion Institute*, vol. 38, pp. 3769–3776, 2021.

[94] J. E. Shepherd and J. Kasahara, "Analytical models for the thrust of a rotating detonation engine," 2017.

[95] J. Koch, M. Kurosaka, C. Knowlen, and J. N. Kutz, "Mode-locked rotating detonation waves: experiments and a model equation," *Physical Review E*, vol. 101, p. 013106, 2020.

[96] J. A. Fay, "Two-dimensional gaseous detonations: velocity deficit," *Physics of Fluids*, vol. 2, pp. 283–289, 1959.

[97] E. K. Dabora, J. Nicholls, and R. Morrison, "The influence of a compressible boundary on the propagation of gaseous detonations," in *Proceedings of Combustion Institute*, vol. 10, pp. 817–830, Elsevier, 1965.

[98] M. Reynaud, F. Virot, and A. Chinnayya, "A computational study of the interaction of gaseous detonations with a compressible layer," *Physics of Fluids*, vol. 29, p. 056101, 2017.

[99] M. Reynaud, S. Taileb, and A. Chinnayya, "Computation of the mean hydrodynamic structure of gaseous detonations with losses," *Shock Waves*, vol. 30, pp. 645–669, 2020.

[100] D. Schwer and K. Kailasanath, "Numerical study of the effects of engine size on rotating detonation engines," *49th AIAA aerospace sciences meeting including the new horizons forum and aerospace exposition*, p. 581, 2011.

[101] J. Sousa, J. Braun, and G. Paniagua, "Development of a fast evaluation tool for rotating detonation combustors," *Appl. Math. Model*, vol. 52, pp. 42–52, 2017.

[102] K. Mazaheri, Y. Mahmoudi, and M. I. Radulescu, "Diffusion and hydrodynamic instabilities in gaseous detonations," *Combustion and Flame*, vol. 159, pp. 2138–2154, 2012.

[103] W. Han, C. Wang, and C. K. Law, "Role of transversal concentration gradient in detonation propagation," *Journal of Fluid Mechanics*, vol. 865, pp. 602–649, 2019.

[104] *Proceedings of the 28th ICDERS*, Institute for Dynamics of Explosions and Reactive Systems, 2022.